

**IMAGE FLOW: GLOBAL GRID TRACKING IN THE IMAGE  
PLANE USING PHOTOGRAMMETRIC APPENDAGE  
STRUCTURAL DYNAMICS EXPERIMENT DATA**

by

**Susan Lynn Linch  
B.S. December 1993, The University of Idaho**

**A Thesis submitted to**

**The Faculty of**

**The School of Engineering and Applied Science  
of The George Washington University in partial satisfaction  
of the requirements for the degree of Master of Science**

**September, 1997**

**Thesis directed by**

**Robert H. Tolson  
Professor of Engineering and Applied Science**

**This research was conducted at NASA Langley Research Center**

## Abstract

The International Space Station requires structural measurements to validate loads, verify mathematical models, and monitor the structural health of appendages. For remote appendages such as solar arrays and thermal radiators, accelerometer measurements are difficult. Therefore, photogrammetric methods were explored for remote structural measurements. The Photogrammetric Appendage Structural Dynamics Experiment was designed to demonstrate photogrammetric methods for remote space station measurements. Video images of the motion of a solar array on the Russian Space Station Mir were digitized, triangulated from image plane time history data into three-dimensional time history data, and analyzed to find structural dynamic parameters of frequencies, damping, and mode shapes. Time histories in the two-dimensional image plane are obtained for several discrete points by tracking solar array features. Traditional tracking algorithms track one feature through time.

This research explores image flow, a global grid tracking algorithm that provides velocity time histories of image plane motion for multiple points on a grid. To use the image flow method for this application, a constant velocity constraint is introduced for various sizes of subimages. Image flow has the advantage of tracking several points on the structure in one analysis while traditional tracking methods only track one feature at a time. Traditional tracking methods require prior selection of features while image flow tracks on a global grid and does not require feature selection. Therefore, the grid selection can be autonomous and the human factor of prior feature selection is not necessary. Image flow also can reduce the local noise experienced by local feature tracking methods by averaging of subimages.

## Acknowledgements

I would like to take this opportunity to thank all of the people who contributed to this project. I would first like to thank my advisors, Dr. Michael G. Gilbert and Dr. Robert H. Tolson. This project would never have been possible without their combined support and heads to bounce ideas off of. I want to thank the members of the PASDE team for providing me insight into a project that I was completely unfamiliar with in the beginning and for making me feel a part of the team.

I would like to give a special thanks to David Cooke for his open door policy, the timely hardware support, the sanity checks, emotional bolstering, and an occasional ice cream treat. I would never have finished this project without him. I would also like to mention my technical reviewers Irene Gregory, Anna Trujillo, and Bill Rosch, who provided invaluable “constructive” criticism, fresh eyes, and a necessary reality check. Thanks also to Stan Husch for graphic help and bearing with me at the end.

Thanks to Russell Shane, Barbara Lakota, and Atherton Carty for making me smile and sticking by me when we all were feeling the crunch of time. A huge hug goes to my parents who have always encouraged me to try anything and who think it's cool to have a rocket scientist for a daughter. Thanks also go to the NASA volleyball gang and the JIAFS crowd for making my stay in Virginia wonderful, memorable, and busy.

# Table of Contents

Abstract.....	ii
Acknowledgements.....	iii
Table of Contents .....	iv
List of Figures .....	vi
List of Tables .....	ix
List of Symbols.....	x
1. Introduction .....	1
2. The Photogrammetric Appendage Structural Dynamics Experiment.....	3
2.1. International Space Station Requirements.....	3
2.2. PASDE Mission Description .....	3
2.3. Data Analysis of the PASDE .....	7
3. Photogrammetric Measurement.....	8
3.1. Tracking in the Image Plane.....	8
3.2. Photogrammetry Equations.....	12
3.3. Modal Analysis: The Eigensystem Realization Algorithm.....	18
4. Image Flow.....	20
4.1. Derivation of Image Flow .....	20
4.2. Modifications and Limitations.....	25
5. Image Flow Analysis and Results.....	30
5.1. Image Flow Applied to a Synthetic Test Image Sequence.....	30
5.2. Image Flow Applied to the PASDE.....	43
6. Conclusions.....	56

<b>References</b> .....	<b>57</b>
<b>A. The Smoothness Constraint of Horn and Schunck</b> .....	<b>A-1</b>
<b>A.1. Derivation of the Smoothness Constraint</b> .....	<b>A-1</b>
<b>A.2. Application to the PASDE</b> .....	<b>A-4</b>
<b>B. Extending the Partial Derivative Estimate</b> .....	<b>B-1</b>
<b>B.1. Expansion to More than Two Pixel Motion</b> .....	<b>B-1</b>
<b>B.2. Testing the Expanded Partial Derivative Estimates</b> .....	<b>B-3</b>

## List of Figures

Figure 1.	STS-74 Shuttle-Mir Docked Configuration: Kvant-II Solar Array and Camera Canister Locations.....	5
Figure 2.	Sample Camera Views for the Post Docking Night Calibration .....	6
Figure 3.	Line Tracking Example.....	9
Figure 4.	Pixel Shift of Subimage A Over Subimage B .....	11
Figure 5.	Geometry of the Camera with Respect to the Imaged Object.....	13
Figure 6.	Photogrammetric Coordinate Systems [after Holmes, 1995] .....	14
Figure 7.	Successive Rotations Around the Coordinate Axes.....	15
Figure 8.	Estimation of Partial derivatives with Central Differences in 3D.....	25
Figure 9.	Example of Subimages Containing Limitation Features .....	27
Figure 10.	Typical Velocity Histogram of One Subimage from a Two-Frame Image Flow Analysis.....	29
Figure 11.	First Frame of Synthetic Image Sequence.....	31
Figure 12.	Successive Grid Scheme: 200x200 Pixel Main Synthetic Image.....	32
Figure 13.	Sample Image Flow Vector Results for 5x5 and 10x10 Grids .....	34
Figure 14.	Velocity Component Results for the 5x5 Subimage Grid .....	35
Figure 15.	Velocity Component Results Corrupted by Noise.....	36
Figure 16.	Partial derivatives of Intensity Averaged Over the First Three Central Differences.....	38
Figure 17.	No Noise Added: Results of Modifications .....	40
Figure 18.	3% Noise Added: Results of Modifications.....	41
Figure 19.	7% Noise Added: Results of Modifications.....	42

Figure 20. First Frame of the PASDE Camera Sequence with the Analysis Grid ..... 44

Figure 21. X-Direction Time Histories of the Kvant-II Solar Array ..... 46

Figure 22. Y-Direction Time Histories of the Kvant-II Solar Array ..... 47

Figure 23. Image for Comparison of Scene Correlation and Image Flow..... 49

Figure 24. Comparison with no Modifications..... 51

Figure 25. Comparison with Modification 1 ..... 52

Figure 26. Comparison with Modifications 1 and 2 ..... 53

Figure 27. Comparison with Modifications 1, 2, and 3 ..... 54

Figure 28. Comparison with Modifications 1 and 3 ..... 55

Figure A.1. Start Frame for the Two Second Tip 6 Image Sequence ..... A-5

Figure A.2. Expanded Detail of Example Subimage ..... A-5

Figure A.3. Frame 3 of Previous Frame Velocity Estimate Analysis..... A-8

Figure A.4. Frame 6 of Previous Frame Velocity Estimate Analysis..... A-8

Figure A.5. Frame 9 of Previous Frame Velocity Estimate Analysis..... A-9

Figure A.6. Frame 13 of Previous Frame Velocity Estimate Analysis..... A-9

Figure A.7. Frame 15 of Previous Frame Velocity Estimate Analysis..... A-10

Figure A.8. Frame 20 of Previous Frame Velocity Estimate Analysis..... A-10

Figure A.9. Frame 3 of Zero Initial Velocity Estimate Analysis ..... A-11

Figure A.10. Frame 6 of Zero Initial Velocity Estimate Analysis ..... A-11

Figure A.11. Frame 9 of Zero Initial Velocity Estimate Analysis ..... A-12

Figure A.12. Frame 13 of Zero Initial Velocity Estimate Analysis ..... A-12

Figure A.13. Frame 15 of Zero Initial Velocity Estimate Analysis ..... A-13

**Figure A.14. Frame 20 of Zero Initial Velocity Estimate Analysis ..... A-13**

**Figure B.1. Expanded Estimation of Partial Derivatives ..... B-3**

**Figure B.2. Comparison of Results from the Chapter 5 Forward Difference  
Method and from the Appendix B Central Difference Method .... B-4**

**Figure B.3. Extended Partial Derivative Component Velocity Results ..... B-5**

## List of Tables

<b>Table 1. STS-74 Mission Events Recorded by the PASDE .....</b>	<b>4</b>
<b>Table 2. PASDE Mission Events Digitized for Further Processing.....</b>	<b>5</b>

## List of Symbols

<b>A</b>	<b>First subimage in image correlation method</b>
$\overline{A}$	<b>Average intensity of subimage A</b>
$A_I$	<b>Object vector in inertial coordinates</b>
$A_{ir}$	<b>Initial amplitude of mode r at location i</b>
<b>a</b>	<b>Image vector in camera coordinates</b>
<b>B</b>	<b>Second subimage for image correlation method</b>
$\overline{B}_{mn}$	<b>Average intensity of subimage B shifted m,n pixels</b>
$CC(m,n)$	<b>Correlation coefficient at a shift of m,n pixels</b>
<b>c</b>	<b>Camera focal length</b>
<b>E</b>	<b>Total error</b>
$E_a$	<b>Error of the image flow equation</b>
$E_b$	<b>Departure from smoothness</b>
$I(x,y,t)$	<b>Intensity of a point in an image pattern</b>
$I_x, I_y, I_t$	<b>Partial derivatives of intensity with respect to (x,y,t)</b>
$i,j$	<b>Pixel location in (y,x)</b>
$i,j,k$	<b>Pixel location in (y,x,t) of image sequence</b>
<b>M</b>	<b>Transformation matrix relating rotated axes to inertial axes</b>
$M,N$	<b>Limits of pixel shift for image correlation method</b>
$m,n$	<b>Pixel shift in (y,x) of image B in relation to image A</b>
$m_v$	<b>Median value of grid velocities</b>
<b>n</b>	<b>Number of iterations</b>
<b>O</b>	<b>Projection center of the photogrammetric system</b>

$P$	Point on the imaged object
$p$	Point $P$ projected onto the image plane
$r,s$	Size of subimage $A$ for image correlation
$u,v$	Image plane components of velocity
$\bar{u},\bar{v}$	Local averages of velocity components
$V$	Magnitude of velocity
$x_i(t)$	Displacement of system at location $i$ and time $t$
$X,Y,Z$	Inertial coordinate system
$X_O,Y_O,Z_O$	Location of projection center ( $O$ ) in inertial coordinates
$X_P,Y_P,Z_P$	Location of object point ( $P$ ) in inertial coordinates
$x,y,t$	Image plane coordinates ( $x,y$ ) through time $t$
$x,y,z$	Camera coordinate system
$x_o,y_o$	Location of projection center ( $O$ ) in camera coordinates
$x_p,y_p$	Location of object point ( $P$ ) projected onto the image plane
$\alpha$	Weighting factor
$\Delta x,\Delta y,\Delta t$	Discrete intervals in image plane coordinates ( $x,y$ ) and time $t$
$\delta_r$	Damping of mode $r$
$\nabla I$	Intensity gradient in image plane coordinates ( $x,y$ )
$\kappa$	Proportionality factor
$\lambda$	Scale factor
$\Omega$	Domain of integration for the smoothness constraint
$\omega_r$	Frequency of mode $r$
$\phi_{ir}$	Initial phase angle of mode $r$ at location $i$

$\sigma$	<b>Standard deviation of subimage intensities</b>
$\sigma(\mathbf{g})$	<b>Standard deviation of subimage intensity gradients</b>
$\theta, \xi, \phi$	<b>Successive rotations about the reference axes</b>

## **Acronyms**

<b>ERA</b>	<b>Eigensystem Realization Algorithm</b>
<b>ISS</b>	<b>International Space Station</b>
<b>PASDE</b>	<b>Photogrammetric Appendage Structural Dynamics Experiment</b>
<b>PRCS</b>	<b>Primary Reaction Control System</b>

# 1. Introduction

Structural measurements of large space structures, such as the planned International Space Station (ISS), are necessary to monitor performance and structural integrity, to improve and validate existing mathematical models, and to confirm that the loads applied are acceptable. Typically, structural measurement is accomplished by measuring displacement, velocity, or acceleration at several locations on the structure with electronic sensors such as accelerometers and strain gauges. Structural dynamic parameters such as frequency, damping, and mode shapes are then extracted from the time histories. However, traditional measurement of some remote ISS appendages is undesirable because of the costs and technical difficulties associated with placing electronic devices on these structures.

Photogrammetric measurement is a versatile, low-cost, low-risk method of remote measurement of appendages that eliminates the wiring and electronics associated with electronic devices. Photogrammetry may be used to target and to measure several different appendages on the ISS, providing versatility. Three-dimensional measurement using photogrammetry requires image sequences from multiple cameras placed in different locations. Structural dynamic parameters are extracted from the image sequences in three steps. First, high contrast features or targets appearing in two or more camera views are tracked to obtain time histories in the image plane. Second, the image plane time histories are triangulated into three-dimensional time histories using geometric parameters of the optical system. Third, a modal parameter identification algorithm is applied to the three-dimensional time histories to find dynamic structural parameters of the imaged object.

Several different methods may be applied to the first part of photogrammetric analysis, tracking points in the image plane. Most tracking methods involve selecting a single high contrast feature such as a line or a spot on the imaged object and tracking the feature as it moves through the image plane. The work presented in this paper describes image flow, an image plane tracking algorithm that recovers image plane time histories on a global grid basis rather than by local feature selection. A global recovery method has three potential advantages: (1) high-contrast features are not required to be selected prior to analysis, (2) time histories of several points on the object may be extracted in one analysis, and (3) the local noise experienced by single feature tracking is reduced by averaging.

Chapter 2 describes the Photogrammetric Appendage Structural Dynamics Experiment (PASDE), an experiment designed to demonstrate photogrammetric measurement of space station appendages. The photogrammetric analysis tools used for the PASDE are presented in Chapter 3. These tools include: (1) two local feature tracking procedures, line tracking and scene correlation, (2) the global grid tracking procedure, image flow, (3) triangulation of image plane time histories into three-dimensional time histories using the geometry of the photogrammetric system, and (4) a modal parameter identification procedure, the Eigensystem Realization Algorithm (ERA). Chapter 4 covers the derivation of image flow and contains a discussion of its advantages and limitations. Image flow is demonstrated in Chapter 5 using a synthetic test problem and is subsequently applied to image data collected by the PASDE.

## **2. The Photogrammetric Appendage Structural Dynamics Experiment**

### **2.1. International Space Station Requirements**

The International Space Station will have accelerometers on the primary U.S. truss but because costs and integration of equipment are prohibitive, accelerometers will not be placed on the solar arrays or the thermal radiators. The PASDE was designed to demonstrate on-orbit photogrammetric measurement techniques as a viable low cost alternative to accelerometers for the ISS. The PASDE flew as a payload on the STS-74 Shuttle docking mission with the Russian Space Station Mir in November, 1995.

The photogrammetric analysis objectives of the PASDE were to prove that photogrammetry may be used for measuring space station appendages and to verify that natural scene contrast may be used in lieu of optical targets. The experiment also shows that routine station events such as jet firings and docking provide sufficient excitation for structural measurement. For demonstration purposes, measurement data was collected from a solar array on Mir that is similar to those planned for the ISS [Gilbert, et al., 1996].

### **2.2. PASDE Mission Description**

The PASDE targeted the Mir Kvant II solar array that is closest to the docked Shuttle during the STS-74 mission. Cameras were placed in three canisters located in Shuttle cargo bays 6, 7, and 13 with two cameras at each location for a total of six PASDE cameras. Figure 1 shows the STS-74 Shuttle-Mir docked configuration with the

location of the camera canisters in the Shuttle cargo bay and the location of the Kvant-II solar array marked. One camera at each location imaged the tip of the array, and the other imaged the root of the array. A sample of the views of the Kvant-II solar array seen from each camera is shown in Figure 2 for one PASDE data recording event, the night calibration performed after docking [Gilbert, et al., 1997].

The experiment had several planned data recording events including docking, jet firings, and solar array slew maneuvers. Video image data was collected for the excitation events shown in Table 1. After return to earth, the video image sequences were digitized for events with high quality data in at least five of the six camera views. The digital image sequences chosen for further processing shown in Table 2 provide sufficient data over the entire solar array for triangulation to three-dimensional time histories and subsequent modal parameter extraction [Gilbert, et al., 1997].

**Mission Event Descriptions**

<p>Camera Alignment and Verification          Post Docking Camera Calibration: Day and Night          Shuttle Docking with Mir          Primary Reaction Control System (PRCS) Test #1          Primary Reaction Control System (PRCS) Test #2          Day to Night Terminator          Night to Day Terminator          Shuttle Mir Attitude Maneuver with Shuttle Primary Jets          PRCS Test #3          Solar Array Sun Track Maneuver #1          Solar Array Sun Track Maneuver #2</p>
---

**Table 1. STS-74 Mission Events Recorded by the PASDE**

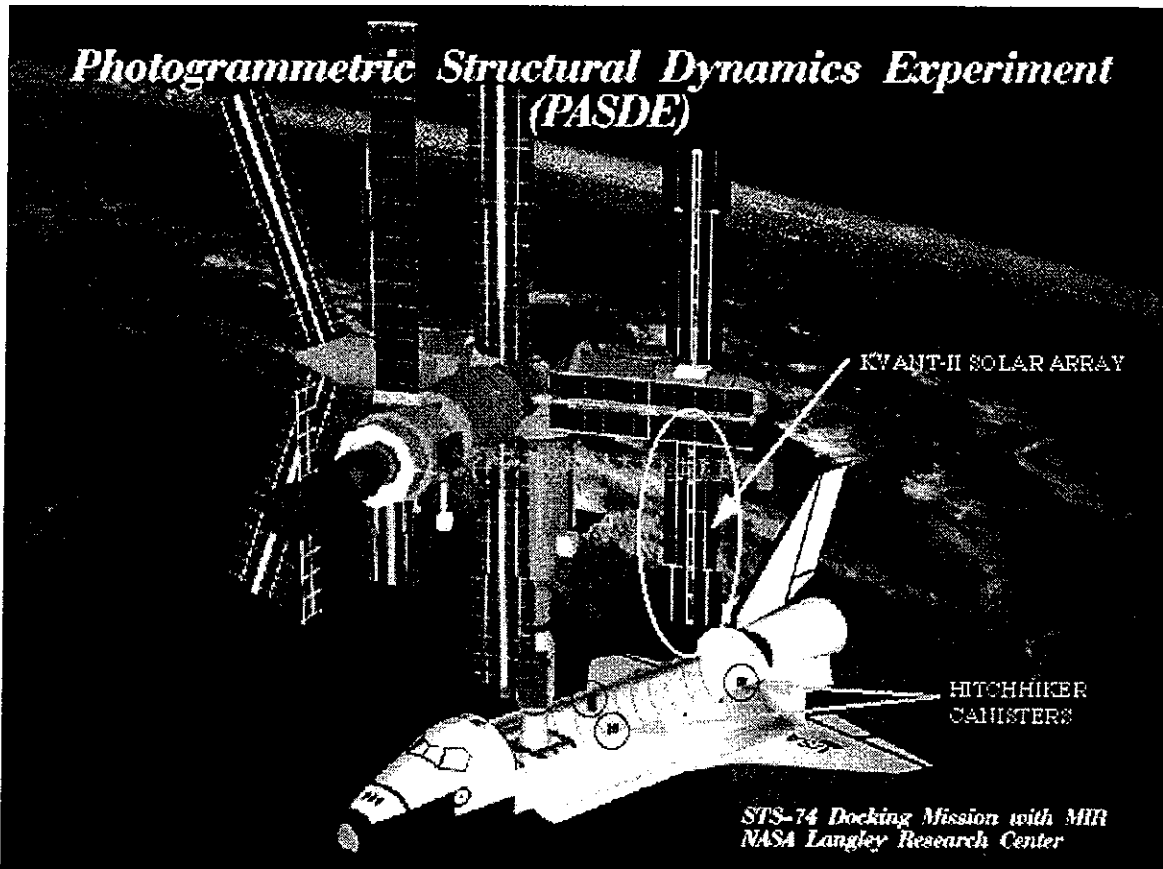
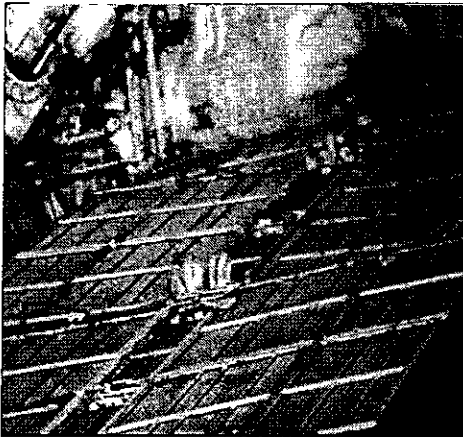


Figure 1. STS-74 Shuttle-Mir Docked Configuration: Kvant-II Solar Array and Camera Canister Locations

Mission Event	Length of Sequence	Number of Cameras
Night/Day Terminator	180 seconds	6
PRCS Test #3, Firing #2	140 seconds	5
PRCS Test #3, Firing #3	60 seconds	5
Solar Array Slew	40 seconds	6

Table 2. PASDE Mission Events Digitized for Further Processing

PASDE Camera Views for the Post Docking Night Calibration



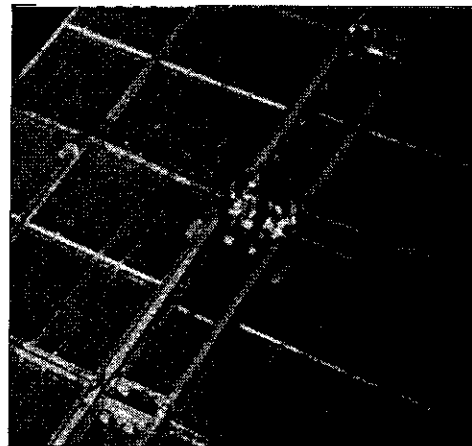
Root Camera, Shuttle Bay Six



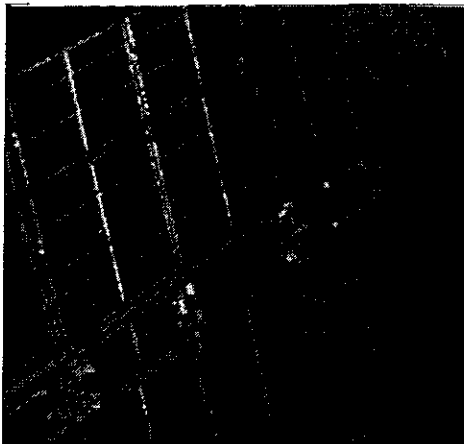
Tip Camera, Shuttle Bay Six



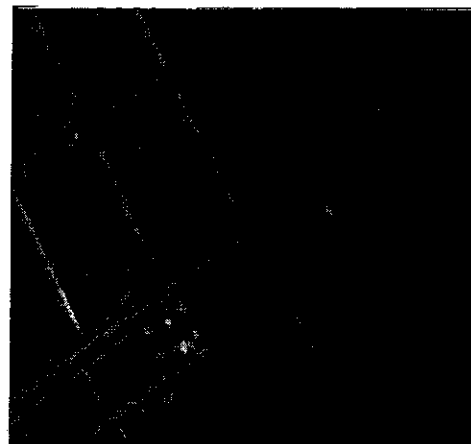
Root Camera, Shuttle Bay Seven



Tip Camera, Shuttle Bay Seven



Root Camera, Shuttle Bay Thirteen



Tip Camera, Shuttle Bay Thirteen

Figure 2. Sample Camera Views for the Post Docking Night Calibration

### **2.3. Data Analysis of the PASDE**

Preliminary analysis of the PASDE image data in Gilbert, et al., [1997], has shown that photogrammetric measurement of space station appendages is feasible for use on the ISS. The digitized image sequences were processed to extract the structural dynamic parameters, frequency, damping, and mode shapes, using the three steps of photogrammetric analysis: (1) tracking in the image plane, (2) triangulation to three-dimensional coordinates, and (3) modal parameter identification. Two local feature methods of tracking in the image plane, line tracking and scene correlation, were explored. Three dimensional displacement time histories were triangulated from image plane time histories generated by the scene correlation method. The ERA was applied to the triangulated time histories to extract structural dynamic parameters of the Kvant-II solar array.

This paper presents image flow as another image plane tracking tool for the PASDE. Additional details of the PASDE data analysis may be found in Gilbert, et al., [1997].

### **3. Photogrammetric Measurement**

The science of photogrammetric measurement is used to analytically relate a two-dimensional targeted object in the image plane to its corresponding location in three-dimensional space. Motion in three dimensions is obtained by tracking and then triangulating points from a sequence of images with a known time interval, or frame rate. Modal identification can then be applied to extract modal parameters.

The first section of this chapter describes several methods of tracking used in the image plane including a brief description of image flow analysis, the object of this study. The basic assumptions, geometry, and triangulation equations of photogrammetry are described in the second section, and the last section contains a brief overview of the ERA, the modal parameter identification algorithm used in the PASDE study.

This research explores the results for the image flow tracking method. Photogrammetric triangulation and modal parameter identification sections are provided for background on photogrammetric measurement. Results of triangulation and modal identification are found in Gilbert, et al., [1997].

#### ***3.1. Tracking in the Image Plane***

##### **3.1.1. Line Tracking and Scene Correlation: Local Feature Tracking**

When dedicated optical targets are not available on the imaged structure, high-contrast, naturally occurring features are tracked through the image sequence instead. For local feature tracking algorithms, the feature to be tracked must be coincident in two or more camera views and must be selected prior to applying the tracking algorithm [Gilbert, et al., 1997].

If the imaged object has naturally occurring high contrast intersecting lines, the line-tracking algorithm may be applicable. Two pairs of points, one pair for each line, are selected. The slope and intercept of each line is calculated from the two pairs of points and the intersection of the two lines is the target point. To find the target point on the next image in the sequence, a line scan of a specified pixel width finds the peak intensity location for each scan line. The centroid values of each scan line peak intensity are found and then a straight line is fit to the respective centroid values for each of the two lines. The new slopes and intercepts are calculated to find the new intersection, or target location. Time histories are generated for the target point using a successive application of this algorithm. Figure 3 is an example of line tracking on the Kvant-II solar array [Welch, 1994]. The two pairs of points used to calculate the slopes and intercepts of the two lines are marked with small X's. The target point at the intersection of the two lines is marked with a large X.

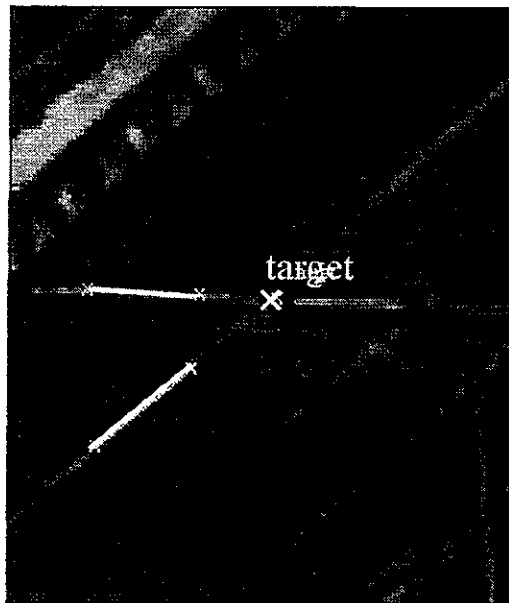


**Figure 3. Line Tracking Example**

The second local feature tracking method is scene or image correlation. The image correlation algorithm matches high contrast features in two or more views by measuring the degree of similarity, or correlation, of an image ( $A$ ) shifted in relation to a second image ( $B$ ). Correlation is at a maximum when the two images are most similar to each other. Figure 4 shows the pixel shift of image  $A$  (size  $r \times s$ ) over image  $B$  for the  $x$ -direction range  $(-M < m < M)$  and the  $y$ -direction range  $(-N < n < N)$ .  $M$  and  $N$  must be chosen to be larger than the expected pixel motion of the object [Pappa, et al., 1995]. The correlation coefficient is calculated as

$$CC(m, n) = \frac{\sum_y \sum_x [B(y + m, x + n) - \bar{B}_{mn}] [A(y, x) - \bar{A}]}{\left[ \sum_y \sum_x [B(y + m, x + n) - \bar{B}_{mn}]^2 \sum_y \sum_x [A(y, x) - \bar{A}]^2 \right]^{1/2}}, \quad (3.1)$$

where

$$\left( i - \frac{(r-1)}{2} \right) \leq y \leq \left( i + \frac{(r-1)}{2} \right), \quad \left( j - \frac{(s-1)}{2} \right) \leq x \leq \left( j + \frac{(s-1)}{2} \right),$$

$\bar{A}$  is the average intensity of subimage  $A$ ,

and  $\bar{B}_{mn}$  is the average intensity of  $B$  shifted by  $(m, n)$  pixels.

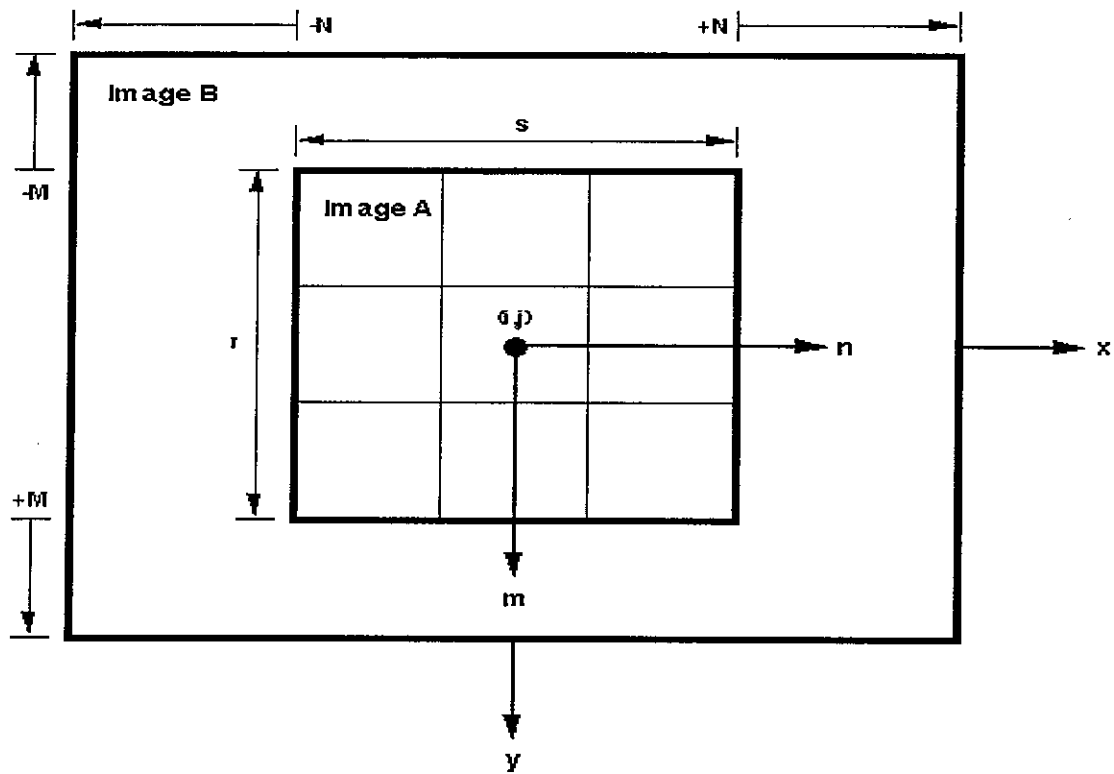


**Figure 4. Pixel Shift of Subimage A Over Subimage B**

Image correlation time histories can be calculated in two different ways. The computationally faster approach is to compare a fixed image with each of the sequence of images following. This approach is computationally simpler and is used to track motions that oscillate around the starting point but does not take rotation or scale changes into account. The second approach compares adjacent pairs of frames sequentially. This method can account for large motions such as solar array slews and general tracking [Pappa, et al., 1995].

### **3.1.2. Image Flow: Tracking on a Global Grid**

Image flow measures apparent image plane velocities of intensity patterns [Horn, et al., 1981]. Intensity patterns may be chosen as subimages in a regularly spaced, global grid. If the points tracked are on a global grid instead of selected as high-contrast points or features on the object, the process may be automated. The global grid may be chosen as convenient to analysis without actually viewing the image data first. The necessity of selecting high contrast features prior to analysis is eliminated. For example, lines for the line tracking method or identifiable target features for the scene correlation method are chosen prior to applying the respective tracking algorithm. The image flow velocity is calculated as a spatial average over each subimage in the grid so local noises associated with local feature tracking are reduced. The image flow algorithm generates velocity time histories for each subimage in the grid, allowing several points on the structure to be tracked in one analysis run. Chapter 4 contains a complete derivation of image flow and Chapter 5 shows the application of image flow to a test problem and to the PASDE data.

## **3.2. Photogrammetry Equations**

### **3.2.1. Assumptions**

Triangulation into three-dimensional coordinates from image coordinates is based on knowing the geometric relationship of the camera with respect to the object imaged. The object is projected onto a two-dimensional image plane where all projected points are assumed to be on the same plane (Figure 5). A point on the object ( $P$ ), its projected point on the image plane ( $p$ ), and the projection center of the system ( $O$ ) must lie on a straight line. Lines drawn from the four corners of the imaged area through the corners

of the image plane intersect at the projection center at a distance of the camera focal length ( $c$ ) from the image plane. The intersection of the image plane and the line drawn from the projection center normal to the image plane is the corresponding point of the projection center in the image plane. For this to be true, atmospheric refraction, lens distortion, and film distortions are either accounted for or neglected in the analysis [Moffitt, 1967].

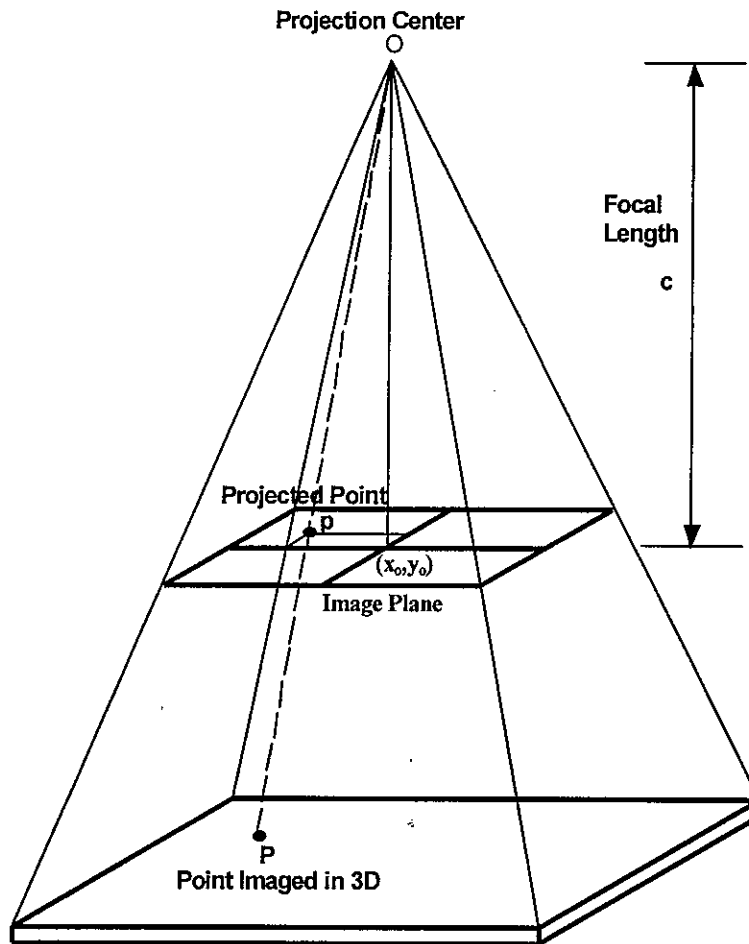
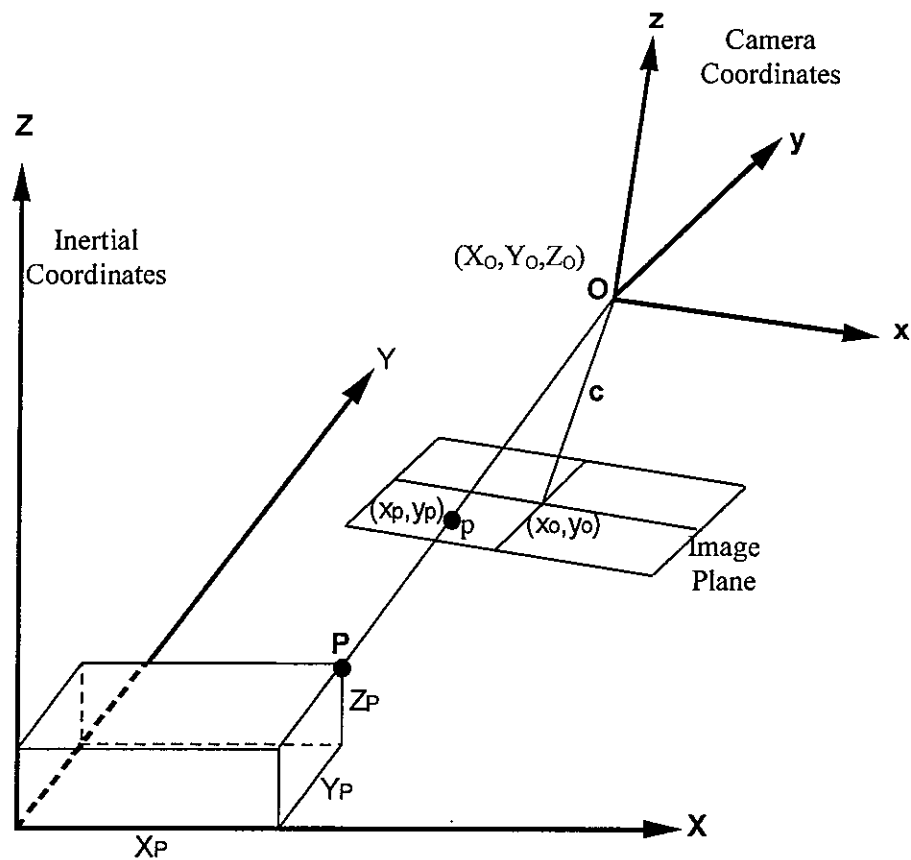


Figure 5. Geometry of the Camera with Respect to the Imaged Object

### 3.2.2. Geometry of the Photogrammetric System

The photogrammetric system consists of a reference coordinate system  $(X, Y, Z)$  and a camera coordinate system  $(x, y, z)$  shown in Figure 6. The origin of the camera

coordinate system is located at the camera projection center ( $O$ ) at  $(X_0, Y_0, Z_0)$  in the reference frame and the imaged point is located at  $(X_p, Y_p, Z_p)$ . The camera focal length ( $c$ ), is the distance of the line perpendicular to the image plane drawn from the camera projection center ( $O$ ) to its corresponding point  $(x_0, y_0)$  on the image plane. The projection location of the imaged point on the image plane is  $(x_p, y_p)$ .



**Figure 6. Photogrammetric Coordinate Systems [after Holmes, 1995]**

Methods of deriving coordinate transformation matrices relating the inertial coordinates to the camera coordinates using a 1-2-3 rotation about the  $X$ ,  $Y$ , and  $Z$  references axes are presented in Kaplan, [1976]. (Figure 7)

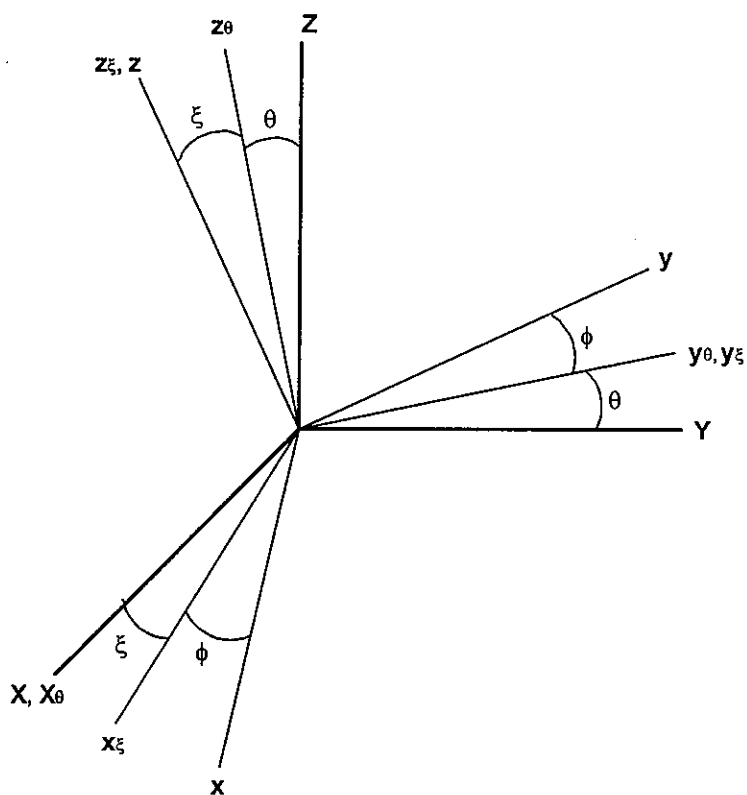


Figure 7. Successive Rotations Around the Coordinate Axes

The first rotation ( $\theta$ ) is defined as the positive rotation about the  $X$  axis with the transformation matrix

$$M_{\theta} = \begin{bmatrix} 1 & 0 & 0 \\ 0 & \cos\theta & \sin\theta \\ 0 & -\sin\theta & \cos\theta \end{bmatrix} \quad \text{where} \quad \begin{bmatrix} x_{\theta} \\ y_{\theta} \\ z_{\theta} \end{bmatrix} = M_{\theta} \begin{bmatrix} X \\ Y \\ Z \end{bmatrix}. \quad (3.2)$$

Similarly, the second rotation ( $\xi$ ) is defined as the positive rotation about the once rotated  $Y$  axis ( $y_{\theta}$ ) with the transformation matrix

$$M_{\xi} = \begin{bmatrix} \cos\xi & 0 & -\sin\xi \\ 0 & 1 & 0 \\ \sin\xi & 0 & \cos\xi \end{bmatrix} \quad \text{where} \quad \begin{bmatrix} x_{\xi} \\ y_{\xi} \\ z_{\xi} \end{bmatrix} = M_{\xi} \begin{bmatrix} x_{\theta} \\ y_{\theta} \\ z_{\theta} \end{bmatrix}. \quad (3.3)$$

The third rotation ( $\phi$ ) is defined as the positive rotation about the twice rotated  $Z$  axis ( $z_\xi$ ) with the transformation matrix

$$M_\phi = \begin{bmatrix} \cos\phi & \sin\phi & 0 \\ -\sin\phi & \cos\phi & 0 \\ 0 & 0 & 1 \end{bmatrix} \quad \text{where} \quad \begin{bmatrix} x \\ y \\ z \end{bmatrix} = M_\phi \begin{bmatrix} x_\xi \\ y_\xi \\ z_\xi \end{bmatrix}. \quad (3.4)$$

Combining Equations (3.2), (3.3), and (3.4) yields

$$\begin{bmatrix} x \\ y \\ z \end{bmatrix} = M_\phi M_\xi M_\theta \begin{bmatrix} X \\ Y \\ Z \end{bmatrix} = M \begin{bmatrix} X \\ Y \\ Z \end{bmatrix}, \quad (3.5)$$

where

$$M = \begin{bmatrix} m_{11} & m_{12} & m_{13} \\ m_{21} & m_{22} & m_{23} \\ m_{31} & m_{32} & m_{33} \end{bmatrix} = \begin{bmatrix} \cos\phi\cos\xi & \sin\phi\cos\theta + \cos\phi\sin\xi\sin\theta & \sin\phi\sin\theta - \cos\phi\sin\xi\cos\theta \\ -\sin\phi\cos\xi & \cos\phi\cos\theta - \sin\phi\sin\xi\sin\theta & \cos\phi\sin\theta + \sin\phi\sin\xi\cos\theta \\ \sin\xi & -\cos\xi\sin\theta & \cos\xi\cos\theta \end{bmatrix} \quad (3.6)$$

All of the parameters required to triangulate from images into three-dimensional space have now been defined. Given a point in the image plane ( $x_p, y_p$ ), calculating its corresponding point in space ( $X_p, Y_p, Z_p$ ) requires that the six translations ( $X_0, Y_0, Z_0, x_0, y_0, c$ ) and the three rotations ( $\theta, \xi, \phi$ ) in at least two cameras of the photogrammetric system be known.

### 3.2.3. Triangulation Equations

The derivation of the triangulation equations depends on the assumption that the point imaged  $(X_P, Y_P, Z_P)$ , its projection point on the image plane  $(x_p, y_p)$ , and the projection center  $(X_O, Y_O, Z_O)$  all lie on the same straight line. The image vector ( $a$ ) and the object vector ( $A_I$ ) are defined as

$$a = \begin{bmatrix} x_p - x_o \\ y_p - y_o \\ -c \end{bmatrix} \quad \text{and} \quad A_I = \begin{bmatrix} X_P - X_O \\ Y_P - Y_O \\ Z_P - Z_O \end{bmatrix}. \quad (3.7)$$

If the straight-line assumption is true, the image vector is related to the object vector by the rotation transformation matrix ( $M$ ) defined in Equation (3.5) and a scale factor ( $\lambda$ ).

$$a = \lambda M A_I \quad \text{or} \quad \begin{bmatrix} x_p - x_o \\ y_p - y_o \\ -c \end{bmatrix} = \lambda M \begin{bmatrix} X_P - X_O \\ Y_P - Y_O \\ Z_P - Z_O \end{bmatrix} \quad (3.8)$$

Divide the first and second equations in the system of equations in (3.8) by the third equation to eliminate the scale factor.

$$\frac{x_p - x_o}{-c} = \frac{m_{11}(X_P - X_O) + m_{12}(Y_P - Y_O) + m_{13}(Z_P - Z_O)}{m_{31}(X_P - X_O) + m_{32}(Y_P - Y_O) + m_{33}(Z_P - Z_O)}$$

$$\frac{y_p - y_o}{-c} = \frac{m_{21}(X_P - X_O) + m_{22}(Y_P - Y_O) + m_{23}(Z_P - Z_O)}{m_{31}(X_P - X_O) + m_{32}(Y_P - Y_O) + m_{33}(Z_P - Z_O)} \quad (3.9)$$

This derivation relating the three-dimensional coordinates of a point to its two dimensional projection for one image results in two equations and three unknowns, so it does not have a unique solution. However, if the same point is imaged in multiple

cameras, the problem becomes overconstrained and can be solved using a least squares approach. For  $i=1$  to  $n$  images and  $j=1$  to  $N$  image points, the triangulation equations in functional form are

$$\begin{aligned} f_{1ij} &= x_{pij} - x_{oi} + c_i \frac{m_{11i}(X_{pj} - X_{oi}) + m_{12i}(Y_{pj} - Y_{oi}) + m_{13i}(Z_{pj} - Z_{oi})}{m_{31i}(X_{pj} - X_{oi}) + m_{32i}(Y_{pj} - Y_{oi}) + m_{33i}(Z_{pj} - Z_{oi})} \\ f_{2ij} &= y_{pij} - y_{oi} + c_i \frac{m_{21i}(X_{pj} - X_{oi}) + m_{22i}(Y_{pj} - Y_{oi}) + m_{23i}(Z_{pj} - Z_{oi})}{m_{31i}(X_{pj} - X_{oi}) + m_{32i}(Y_{pj} - Y_{oi}) + m_{33i}(Z_{pj} - Z_{oi})} \end{aligned} \quad (3.10)$$

where the sums of the squares of  $f_{1ij}$  and  $f_{2ij}$  are minimized by the least squares solution [Holmes, 1995].

### **3.3. Modal Analysis: The Eigensystem Realization Algorithm**

Modal identification is the process by which time history measurements of the structure are decomposed into structural dynamic parameters frequency, damping, and mode shapes. The parameters are then used to update analytical models and may help predict the response of the structure to other excitations.

The ERA is a state-space realization technique performed in the time domain that uses time histories at multiple points to determine the dynamic parameters. ERA analysis is based on free decay vibration response of a linear system. Equation (3.11) is used to describe the system [Gilbert, et al., 1997].

$$x_i(t) = \sum_{r=1}^M A_{ir} e^{\delta_r t} \sin(\omega_r t + \varphi_{ir}) \quad (3.11)$$

The ERA is used to determine the unknown parameters of the number of modes excited, the initial amplitude of mode  $r$  at measurement location  $i$ , the initial phase angle of the mode  $r$  at measurement location  $i$ , the frequency of mode  $r$ , the damping of mode  $r$

The ERA is a simultaneous analysis of multiple measurements. For a noisy system, the set of parameters found by the ERA is a best-fit approximation in a least-squares sense. For a complete derivation of the ERA see Juang, [1994].

## 4. Image Flow

Image flow is a measure of the apparent velocity of an intensity pattern through a sequence of images. The image flow tracking algorithm provides a method of recovering image plane time histories over the entire imaged object rather than for selected local features on the imaged object. Local feature tracking techniques such as the line tracking and cross-correlation methods described in Chapter 2 calculate image plane motion data for a single, high-contrast object point or feature. Local recovery of motion requires the analyst to select the high contrast spot or line prior to analysis while image flow recovers the image plane motion of subimages on a convenient global grid chosen by the analyst and prior selection of high contrast, local features is not required. Image flow analysis recovers image plane motion data for several points on the object in one analysis while the local feature tracking methods use several analyses, one for each feature tracked, to recover a comparable set of image plane time histories. Global tracking methods also have the potential to reduce the local noise experienced by local feature tracking methods because the flow velocity is calculated as a spatial average for each subimage in the grid, so local noises are averaged and their effects are diminished.

### ***4.1. Derivation of Image Flow***

#### **4.1.1. Image Flow Equations**

As an image pattern or set of object points moves through an image sequence, a point on the object has the intensity  $I(x,y,t)$ . Assuming the intensity of each of these object points in the image pattern is constant through successive frames, the substantial derivative of intensity in Equation (4.1) with respect to time is zero.

$$\frac{DI}{Dt} = 0. \quad (4.1)$$

Even though the intensity of an object point within an image pattern remains constant with respect to the image pattern, the set of object points moves with respect to the image plane. Therefore, the intensity of a pixel in the image plane is not constant through time and a total differential of image plane motion can be defined. The total differential is defined in Rektorys, [1969], and is applied to intensity  $I$  at point  $(x,y,t)$  in image plane coordinates as

$$dI = \frac{\partial I}{\partial x} dx + \frac{\partial I}{\partial y} dy + \frac{\partial I}{\partial t} dt. \quad (4.2)$$

Divide by  $dt$  to get

$$\frac{DI}{Dt} = \frac{\partial I}{\partial x} \frac{dx}{dt} + \frac{\partial I}{\partial y} \frac{dy}{dt} + \frac{\partial I}{\partial t}, \quad (4.3)$$

define the image plane components of velocity  $u$  and  $v$  as

$$u = \frac{dx}{dt} \quad \text{and} \quad v = \frac{dy}{dt}, \quad (4.4)$$

introduce the notation  $I_x$ ,  $I_y$ , and  $I_t$  for the partial derivatives of intensity with respect to  $x$ ,  $y$ , and  $t$ , and rewrite Equation (4.3) such that

$$I_x u + I_y v + I_t = 0 \quad (4.5)$$

[Horn, et al., 1981].

Equation (4.5) is the basis for all of the image flow analyses found in this study, where the image plane velocity components  $u$  and  $v$  are the unknowns to be calculated. Additional constraints found in Section 4.1.2 must be introduced at this point because the velocity field has two components  $(u, v)$  of motion for each point in the intensity pattern and these cannot be uniquely determined by Equation (4.5).

#### 4.1.2. Constraints

Other image flow work addresses a smoothness constraint in which a point on the imaged object and its neighboring points are assumed to have similar velocities. The smoothness constraint found in Horn, et al., [1981], may be used to find the general trend in motion of an object in the image sequence and to make a qualitative assessment of the contrast features of the object. The smoothness constraint analysis highlights the ability of the image flow tracking algorithm to detect flow velocities of the high contrast features over the entire image through time. However, the smoothness constraint is not applicable to quantitatively measuring the velocities for use in subsequent triangulation into three-dimensional time histories. The smoothness constraint was applied to the PASDE data to illustrate general motion and the contrast features of the Kvant-II solar array. See Appendix A for a derivation of the smoothness constraint and results of smoothness constraint analysis of the PASDE data.

To find accurate, quantitative measurements of image flow velocity, a constant velocity constraint is introduced. A point on an elastic structure is not free to move independently of its neighboring points. For the application of structural motion of space station appendages, a small representative area of the structure is assumed to move with a rigid body motion  $(x, y)$  in the image plane. Because structural vibrations of these

appendages are expected to be small in relation to the size of the structure, the assumption that a point on the appendage and its adjacent points are moving as rigid body translations  $(x,y)$  in the image plane is valid. Rigid body rotations of the solar array are neglected in this study because component motions are at least two orders of magnitude smaller than the length of the solar array. However, rotations may be considered in other dynamic applications of image flow.

The point and its adjacent points are therefore moving together with an average constant velocity. If the image plane is divided into a grid of small enough subimages, each subimage is assumed to move with a constant average velocity. The image flow velocity of the center pixel of each subimage is recovered as the average velocity of the subimage. To have an accurate representation of the constant velocity constraint, the subimage should be as small as possible. However, if the subimages are too small, spatial averaging and contrast variations are sacrificed. For each subimage, the components  $(u,v)$  of velocity are held constant, and the image flow Equation (4.5) is rewritten in matrix form.

$$\begin{bmatrix} I_x & I_y \end{bmatrix} \begin{bmatrix} u \\ v \end{bmatrix} = -[I_t] \quad (4.6)$$

The average constant velocity components  $(u,v)$  over the subimage are then calculated as a least squares solution. The constant velocity constraint was used in this study to quantify time history data in the image plane for application to large, vibrating space structure appendages.

### 4.1.3. Estimating Partial Derivatives of Intensity

The partial derivatives of intensity ( $I_x$ ,  $I_y$ , and  $I_t$ ) must be estimated using discrete image sequence pixel intensity data to compute the components of velocity ( $u, v$ ). A Taylor series expansion provides a computationally simple estimation of the first derivative in one dimension.

$$f(x + \Delta x) = f(x) + \frac{\Delta x f'(x)}{1!} + \frac{(\Delta x)^2 f''(x)}{2!} + \frac{(\Delta x)^3 f'''(x)}{3!} + \dots \quad (4.7)$$

The first order forward difference is found by neglecting the terms higher than  $f'(x)$  and solving for  $f'(x)$  [Hornbeck, et al., 1975].

$$f'(x) = \frac{f(x + \Delta x) - f(x)}{\Delta x} \quad (4.8)$$

Similarly, the first order forward difference is

$$f'(x) = \frac{f(x) - f(x - \Delta x)}{\Delta x} \quad (4.9)$$

Add Equations (4.8) and (4.9) to obtain the second order central difference.

$$f'(x) = \frac{f(x + \Delta x) - f(x - \Delta x)}{2\Delta x} \quad (4.10)$$

A method for using Equation (4.10) in three-dimensions is presented in Horn, et al., [1981]. Figure 8 is a cube representing 2 pixels in each dimension. A simple method of estimation is to use two pixels in each direction. For this case, the measurement  $x, y, t$  is actually calculated at the center of the cube ( $i+1/2, j+1/2, k+1/2$ ). Since this is not a pixel location, the partial is applied to the pixel location ( $i, j, k$ ). Each partial at location ( $i, j, k$ ) is calculated in Equation (4.11) as an average of the first four adjacent central differences in the cube in Figure 8.

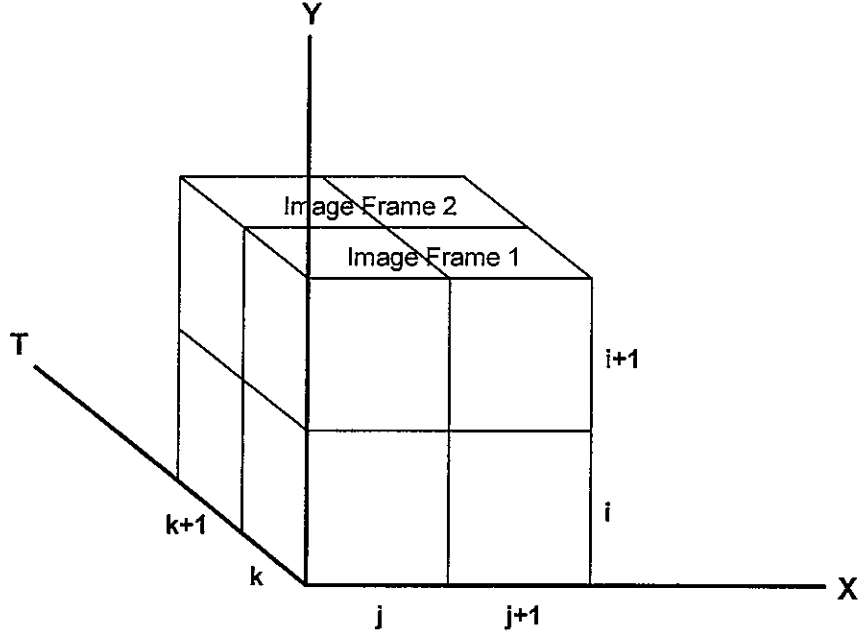


**Figure 8. Estimation of Partial with Central Differences in 3D**

$$I_x = \frac{1}{4\Delta x} (I_{i,j+1,k} - I_{i,j,k} + I_{i+1,j+1,k} - I_{i+1,j,k} + I_{i,j+1,k+1} - I_{i,j,k+1} + I_{i+1,j+1,k+1} - I_{i+1,j,k+1})$$

$$I_y = \frac{1}{4\Delta y} (I_{i+1,j,k} - I_{i,j,k} + I_{i+1,j+1,k} - I_{i,j+1,k} + I_{i+1,j,k+1} - I_{i,j,k+1} + I_{i+1,j+1,k+1} - I_{i,j+1,k+1}) \quad (4.11)$$

$$I_t = \frac{1}{4\Delta t} (I_{i,j,k+1} - I_{i,j,k} + I_{i+1,j,k+1} - I_{i+1,j,k} + I_{i,j+1,k+1} - I_{i,j+1,k} + I_{i+1,j+1,k+1} - I_{i+1,j+1,k})$$

Equation (4.11) is a simple method of estimating the first derivative in three dimensions. This estimate has the advantage of being computationally simple and a more involved method of estimation is not required for most applications.

## **4.2. Modifications and Limitations**

The first limitation of the image flow algorithm is the estimation of the partial derivatives ( $I_x$ ,  $I_y$ , and  $I_t$ ) calculated in Equation (4.11). The current estimate scheme will result in inaccurate calculations of image flow components if the framewise pixel motion in either component direction is more than one pixel for some image characteristics. If

the intensity ( $I$ ) is not a smooth transition over more than two pixels, the intensity function does not vary linearly and the estimation of in Equation (4.11) is inadequate and must be expanded. For the application to the PASDE data, the estimate in Equation (4.11) will suffice because the framewise pixel motion of the Kvant-II solar array does not exceed the one-pixel limitation for the image sequence chosen to illustrate the method. Methods of extending the partial derivative estimate over a larger range of pixels are shown in Appendix B, thus extending the range of motion the object can have in a two-frame sequence. This estimate extension is not required if the rate of data collection can be changed to force the motion to fall within the one pixel limit but sometimes the experiment hardware will not allow this option.

Second, consider the nature of the intensity data. If the image is divided into a grid of subimages, some of the subimages contain little or no contrast. Figure 9 is an example of the test image sequence used in Chapter 5 and will be used for examples of the image flow limitations. See cells 1, 4, 5, and 21 in Figure 9 for examples of subimages with little or no contrast. These subimages that contain almost no change in intensity in either component direction do not provide accurate results and are excluded from the image flow analysis. To eliminate subimages with little or no contrast, the standard deviation of the pixel intensity values of the main image is compared to the standard deviation of each of the subimages. If the subimage standard deviation is less than fifteen percent of the main image standard deviation of intensity, that subimage is excluded from the image flow analysis. For PASDE data analysis, fifteen percent is the threshold that preserves useful data while discarding most low contrast problem areas. Other data sets may require a different threshold.

The third limitation stems from the intensity gradient or change in intensity of a subimage. See cells 8, 12, 13, and 14 in Figure 9 for examples of subimages with a gradual gradient. If the change in intensity is gradual with no high-contrast features or abrupt changes, the image flow algorithm accurately calculates the component velocities in synthetic data with no noise. However, these gradual gradient areas do not produce accurate velocity results for noisy image data. To deal with this limitation, the gradient of intensity is calculated at each pixel local in the subimage. The standard deviation of the pixel intensity gradient values is calculated for every subimage in the grid. If the standard deviation of intensity gradient values of a subimage is less than fifty percent of the mean of all of the intensity gradient standard deviations in the grid, then that subimage is excluded from the image flow analysis.

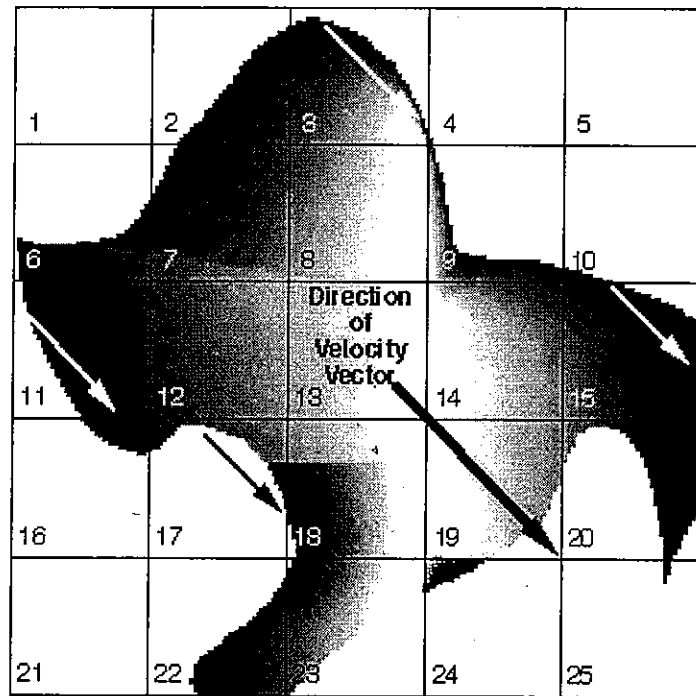


**Figure 9. Example of Subimages Containing Limitation Features**

The fourth limitation in image flow analysis deals with the shape and position of the high contrast features. If a high contrast edge is oriented so that it is almost parallel to the image flow velocity vector, the image flow algorithm will detect little apparent motion in that particular area of the image. See cells 3, 11, 15, and 17 in Figure 9 for examples of subimages that illustrate the feature orientation limitation. To deal with this problem, a histogram approach is used. Figure 10 shows an example histogram of velocities obtained from the synthetic test sequence for the no noise case in Chapter 4. This histogram is a typical velocity distribution for the noise cases and for the PASDE data analysis. If the expected values are  $u=1$  and  $v=1$ , Figure 10 shows that velocities in subimages containing orientation limitation features are underestimated. For the PASDE data analysis, the subimages containing velocities less than the median value of the velocity distribution are also excluded from the image flow analysis. This is done to discard most underestimated velocities. Other data sets may use a different threshold.

The second, third and fourth limitations are explained in detail in Chapter 5. The modifications presented here were found by experimentation in the test image analysis and were subsequently applied to the PASDE data analysis. For automated application to the ISS, common thresholds should be explored to apply to all imaged arrays.

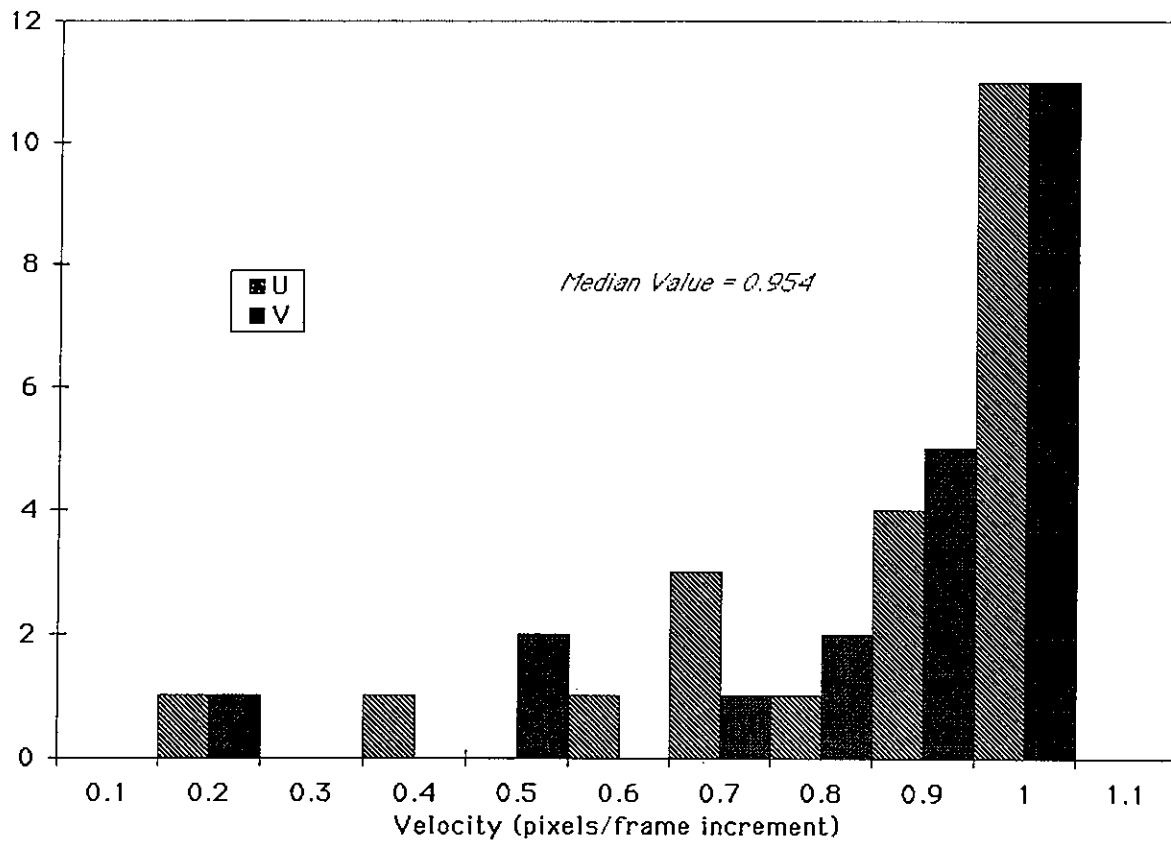


**Figure 10. Typical Velocity Histogram of One Subimage from a Two-Frame Image Flow Analysis**

## 5. Image Flow Analysis and Results

### 5.1. *Image Flow Applied to a Synthetic Test Image Sequence*

The image flow method was first tested on synthetic image data to illustrate capabilities and limitations and to determine the best way to apply the image flow algorithm to a PASDE image sequence. Testing the synthetic image sequence involved six steps: (1) a synthetic image sequence was created, (2) an analysis grid of subimages was chosen for image flow measurement locations, (3) image flow results were found for the subimage grid, (4) random noise was added to the image data to determine the sensitivity of the image flow algorithm to less than optimal data, (5) limitations of the image flow algorithm were identified, and (6) modifications were implemented to correct the limitations.

#### 5.1.1. **The Synthetic Test Image Sequence: Specifications**

The synthetic image sequence created in step one of the testing process contains a rigid test object shifted in pixel increments to simulate motion through the sequence. Since the PASDE image data has 256 levels of intensity, the synthetic image was designed to have the same range of 256 intensity levels. Figure 11 is the first frame of the test image sequence containing the rigid test object. The test object has abrupt contrast features including edges and intensity gradients that cover the entire range of 256 intensity levels. The high-contrast features of the object are varied with different edge orientations and intensity gradients. Three main features of the test object illustrate limitations of the image flow algorithm: (1) areas of little or no intensity gradient, (2)

areas with a gradual intensity gradient, and (3) irregular edges that are almost parallel to the object motion.

Simulated diagonal motion was used to capture both components of velocity  $(u,v)$ . The synthetic test sequence is a two-frame, diagonal motion image sequence where the object is shifted one pixel in the positive x-direction and one pixel in the positive y-direction. Appendix B contains simulations with object motion greater than one pixel in either component direction.

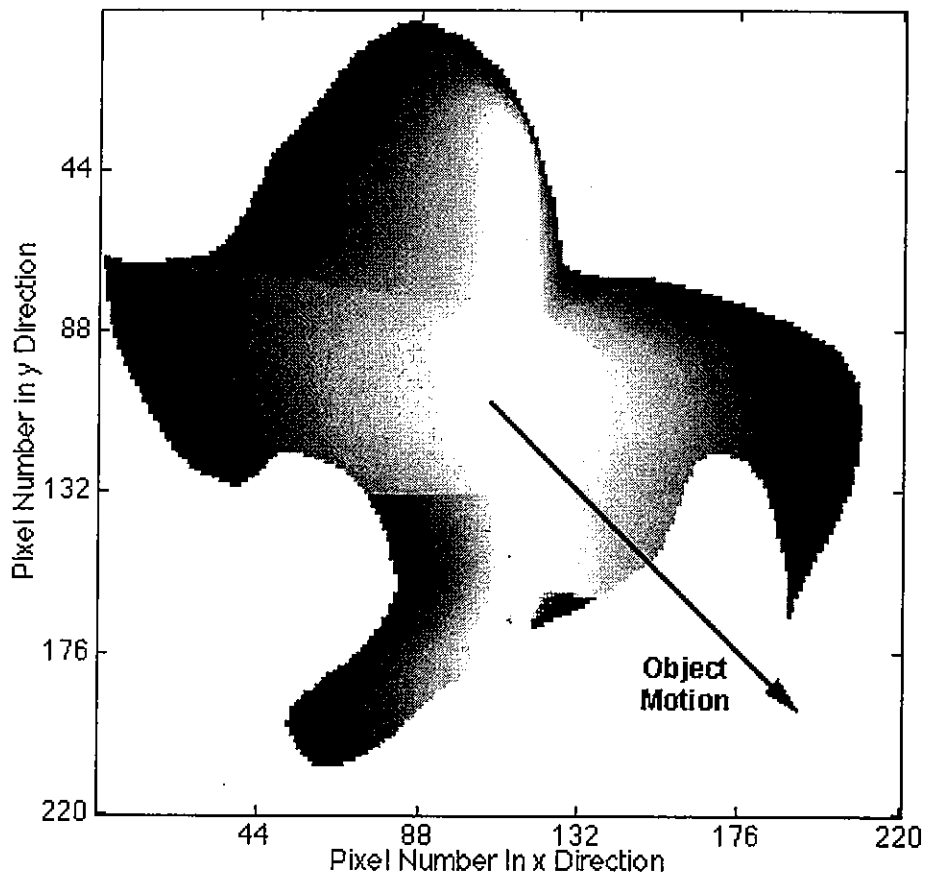


**Figure 11. First Frame of Synthetic Image Sequence**

### 5.1.2. Choosing the Analysis Grid of Image Flow Measurement Locations

A successive grid scheme analysis was used to determine the subimage size necessary to accurately capture the image plane velocities of the test object. Figure 12 is an example of a successive grid scheme used in the grid analysis. Image plane velocities are calculated for successive divisions (Figure 12b-d) of the main grid (Figure 12a) until the divisions no longer produce accurate results.

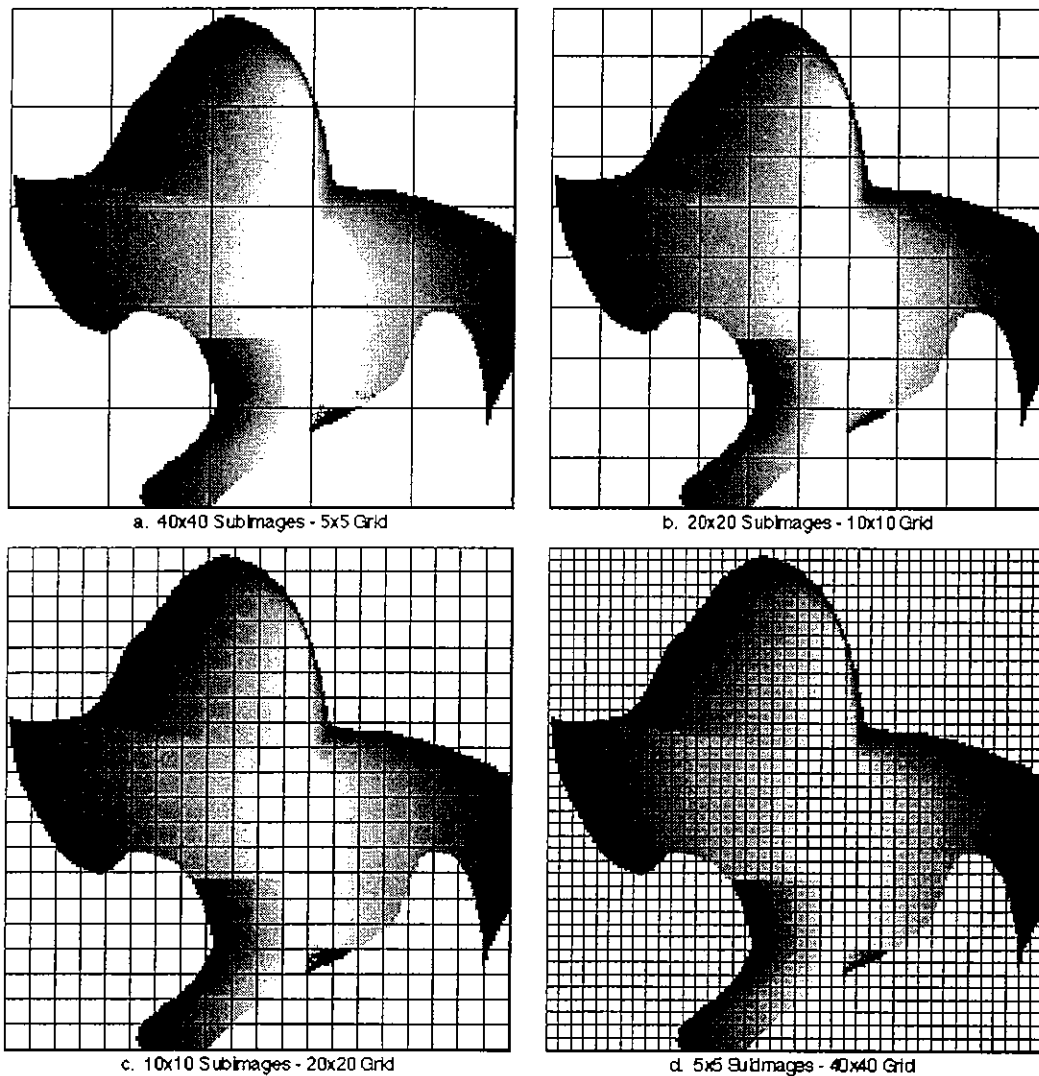


Figure 12. Successive Grid Scheme: 200x200 Pixel Main Synthetic Image

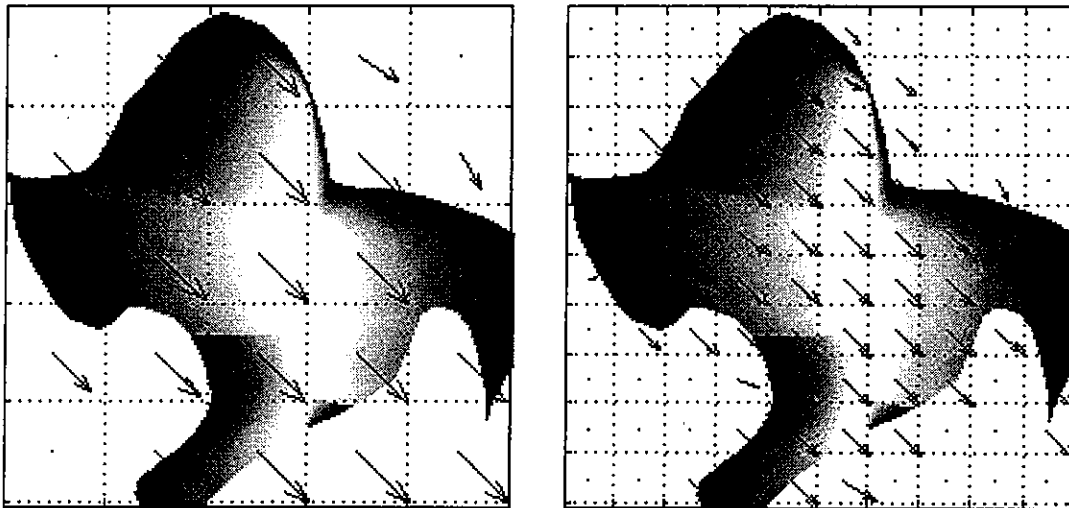
After experimenting with grids varying from 2x2 subimages to 100x100 subimages, a range of acceptable subimage grid sizes was determined. Subimages of more than 7-10% of the total image size produced the most accurate results. This corresponds to a subimage size of at least 14x14 pixels. The main grid division was also chosen to have at least 16 analysis points or a 4x4 subimage grid. These subimage sizes are rules of thumb that were developed on the test image sequence. The same subimage size ranges were then tested on the PASDE data and were found to be acceptable. However, other data sets may require a different range of subimage sizes.

### 5.1.3. Results of Image Flow Applied to the Test Sequence

The image flow algorithm was applied to the test sequence of one diagonal pixel motion for the grid scheme illustrated in Figure 12 to determine how accurately image flow quantifies image plane velocities between two successive frames of image data. In the case of the synthetic, two-frame image sequence chosen, the expected velocity components ( $u, v$ ) for one diagonal pixel motion are calculated as:

$$\begin{aligned}
 u &= \frac{\Delta x}{\Delta t} = \frac{1 \text{ pixel}}{1 \text{ time unit}} = 1 \frac{\text{pixel}}{\text{time unit}} \\
 v &= \frac{\Delta y}{\Delta t} = \frac{1 \text{ pixel}}{1 \text{ time unit}} = 1 \frac{\text{pixel}}{\text{time unit}}
 \end{aligned}
 \tag{5.1}$$

To show the velocity results pictorially, the average velocities for each subimage in a given grid are plotted as vectors and scaled to fit their respective subimages. Figure 13 shows the vector plots for the first two subimage grids from Figure 12. If the vector points to the bottom right corner of the subimage, the image flow algorithm correctly determined the image plane expected velocities for the subimage.



a. 40x40 Subimages - 5x5 Grid      b. 20x20 Subimages - 10x10 Grid

**Figure 13. Sample Image Flow Vector Results for 5x5 and 10x10 Grids**

The numerical results are shown along with the vector plots in Figure 14 for the velocity components  $(u, v)$  of the 5x5 subimage grid. The grid is numbered as cells 1 through 25. The numerical results illustrate the limitations of the image flow method. To quantify the accuracy of the results and to develop the thresholds for the modifications presented in Chapter 4, a ten percent criteria was chosen where the expected values of the velocity components are  $u=1$  and  $v=1$ .

$$0.9 \leq \left( \frac{u+v}{2} \right) \leq 1.1 \quad (5.2)$$

In Figure 14, cells 2, 6, 7, 8, 12, 13, 14, 18, 19, 20, 22, 23, 24, and 25 satisfy the criteria in Equation (5.2). Cells 1, 4, 5, and 21 illustrate the second limitation of little or no contrast outlined in Chapter 4 and do not satisfy the criteria. Cells 3, 9, 10, 11, 15, 16, and 17 illustrate the fourth limitation of parallel features from Chapter 4. Notice that in the absence of noise, the third limitation of gradual gradient (cells 8, 12, 13, and 14) is not detected and these cells satisfy the criteria.

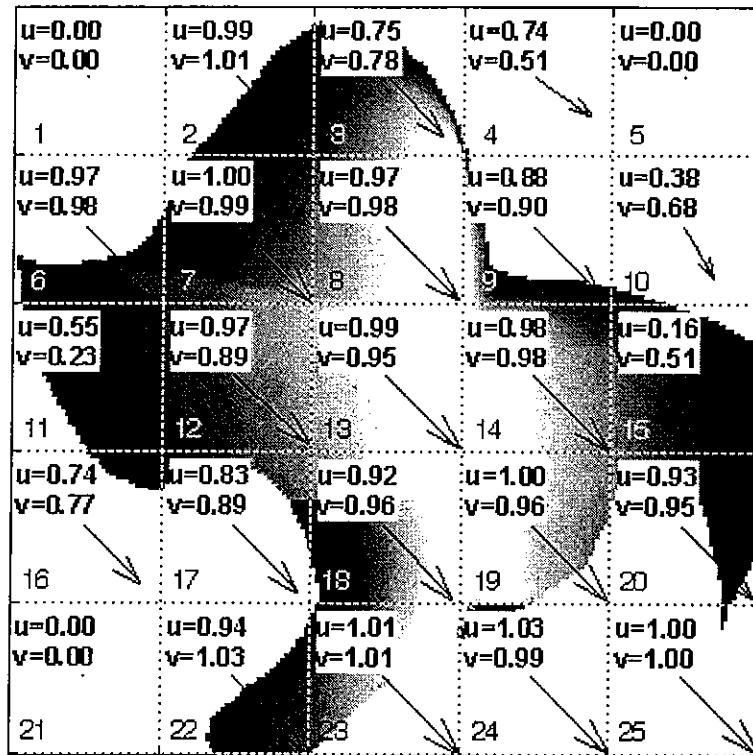
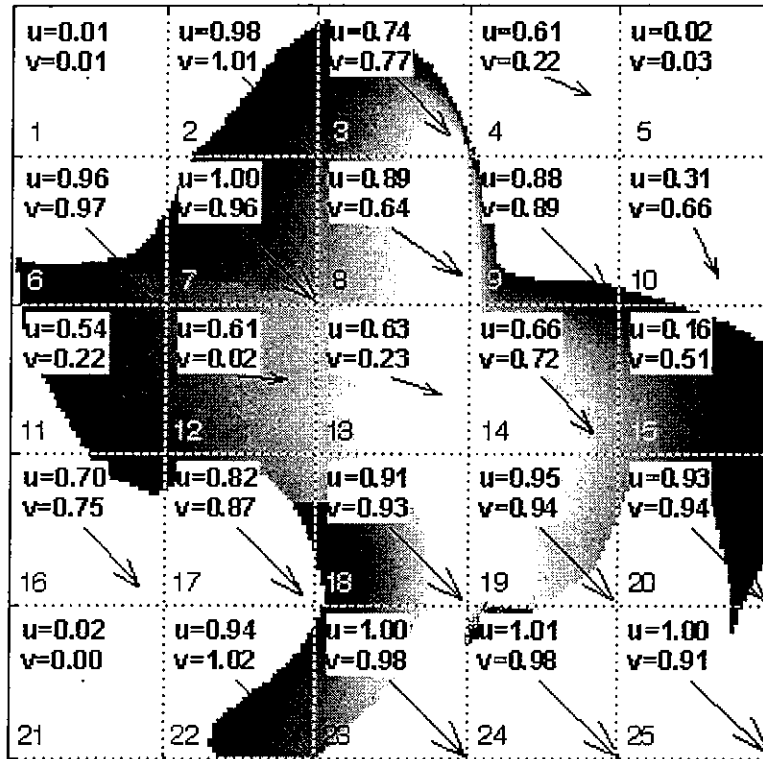


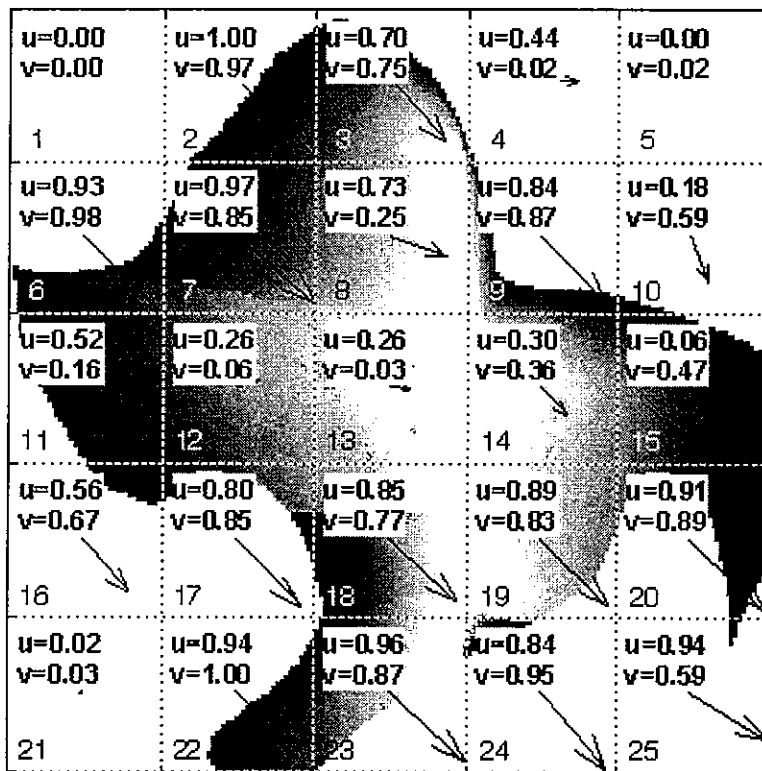
Figure 14. Velocity Component Results for the 5x5 Subimage Grid

#### 5.1.4. Sensitivity of the Image Flow Algorithm to Noise

To test the sensitivity of the image flow algorithm to noise the data was corrupted by  $\pm 3\%$  and  $\pm 7\%$  uniformly distributed random noise calculated as a percentage of 256 levels of intensity. Numerical results of the random noise analyses are shown in Figure 15. Compare these results to the results of the noise free case (Figure 14). The noise has very little effect in subimages with (1) no intensity changes, e.g. cells 1, 5, and 21, or (2) abrupt changes in intensity, e.g. cells 2, 3, 6, 7, 9, 11, 15, 16, 17, 19, 20, 22, 23. The addition of noise has a large impact on the velocity results of (1) the subimages with gradual intensity gradients, e.g. cells 8, 12, 13, 14, and 18, and (2) the subimages that contain only a small portion of the moving object, e.g. cells 4, 10, 24, and 25.



a. Corrupted by 3% Noise



b. Corrupted by 7% Noise

Figure 15. Velocity Component Results Corrupted by Noise

The noise cases show the importance of including modifications for image flow limitations. In the test image, 22 of 25 cells contain portions of the synthetic object. Of these 22 cells, 14 cells satisfy the criteria in Equation (5.2) in the noise free case (Figure 14), 10 cells satisfy the criteria in the 3% noise case (Figure 15a), and 6 cells satisfy the criteria in the 7% noise case.

### 5.1.5. Modifications for Limitations to the Image Flow Algorithm

The image flow algorithm was modified to deal with the three limitations of little or no contrast, gradual gradients, and high-contrast feature orientation. The first modification corrects for little or no contrast in a subimage. The standard deviation of the intensities is calculated for each subimage in the grid ( $\sigma_{subimage}$ ). If  $\sigma_{subimage}$  is less than 15% of the standard deviation of the intensities of the total image ( $\sigma_{total}$ ), the subimage is excluded from the image flow analysis by setting  $u$  and  $v$  equal to zero.

$$\begin{aligned} &\text{if } \sigma_{subimage} < (0.15 * \sigma_{total}), \\ &u_{subimage} = 0 \quad \text{and} \quad v_{subimage} = 0. \end{aligned} \quad (5.3)$$

The second modification eliminated problem areas due to gradual intensity gradients that are subject to noise effects. The intensity gradient is calculated as

$$gradI = \frac{\partial I}{\partial x} e_x + \frac{\partial I}{\partial y} e_y. \quad (5.4)$$

where  $e_x$  and  $e_y$  are unit vector in directions  $x$  and  $y$ , respectively. The partials of intensity with respect to  $x$  and  $y$  are calculated as second order central differences averaged over the first three central differences in a square (Figure 16).

$$\begin{aligned} \frac{\partial I}{\partial x}(i, j) &= \frac{1}{3}[I(i+1, j+1) - I(i+1, j-1) + I(i, j+1) - I(i, j-1) + I(i-1, j+1) - I(i-1, j-1)] \\ \frac{\partial I}{\partial y}(i, j) &= \frac{1}{3}[I(i+1, j+1) - I(i-1, j+1) + I(i+1, j) - I(i-1, j) + I(i+1, j-1) - I(i-1, j-1)] \end{aligned} \quad (5.5)$$

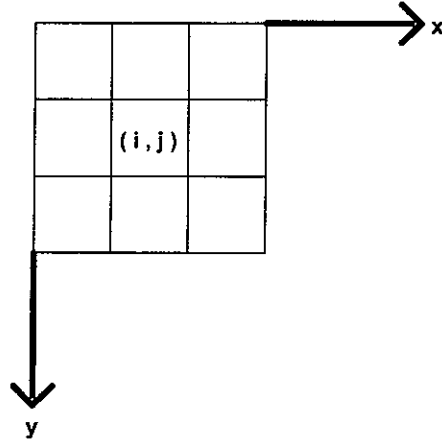


**Figure 16. Partial of Intensity Averaged Over the First Three Central Differences**

The partials estimated in Equation (5.5) are image plane averages and are not averaged over time so are different from the partials estimated in Equation (4.11). This calculation is performed first to determine subimages that can be excluded from the analysis. Using the estimated partials in Equation (5.5), the gradients are then compared as a scalar calculated as

$$G(i, j) = \left| \frac{\partial I}{\partial x} \right| + \left| \frac{\partial I}{\partial y} \right|. \tag{5.6}$$

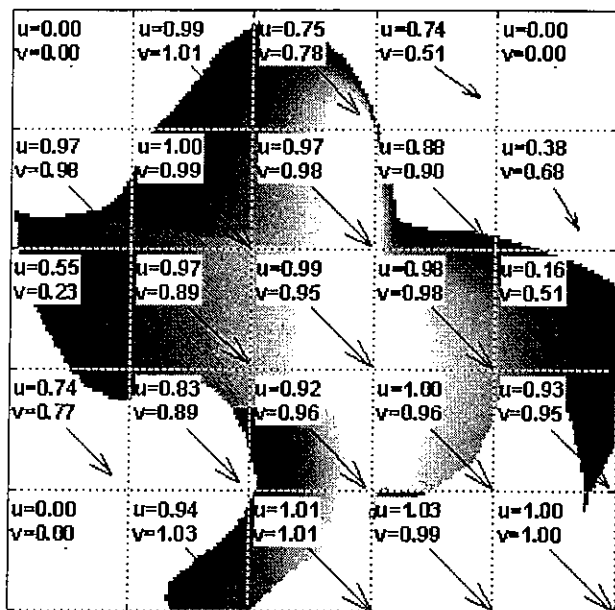
The standard deviation of the scalar gradient ( $G$ ) in Equation (5.6) is calculated for each subimage and compared to the mean of all of the subimage scalar gradient standard deviations. If the scalar gradient standard deviation of a subimage ( $\sigma^{(g)}_{subimage}$ ) is less than fifty percent of the mean scalar gradient standard deviation ( $\sigma^{(g)}_{mean}$ ), that subimage is excluded from the image flow analysis by setting  $u$  and  $v$  equal to zero.

$$\begin{aligned} &\text{if } \sigma^{(g)}_{subimage} < (0.5 * \sigma^{(g)}_{mean}), \\ &v_{subimage} = 0 \text{ and } u_{subimage} = 0. \end{aligned} \tag{5.7}$$

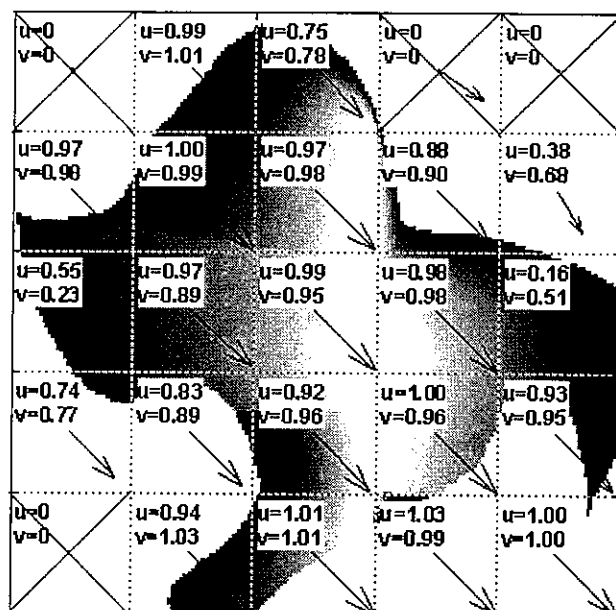
The third modification deals with features that have an orientation paralleling the image flow vector. This modification is applied after the first two modifications have been implemented. The median ( $m_v$ ) of the magnitudes ( $V_{subimage}$ ) of the nonzero velocities is calculated. Subimages with velocity magnitudes that are less than this median value are excluded from the image flow analysis by setting  $u$  and  $v$  equal to zero.

$$\begin{aligned} &\text{if } V_{subimage} < m_v, \\ &u_{subimage} = 0 \text{ and } v_{subimage} = 0. \end{aligned} \quad (5.8)$$

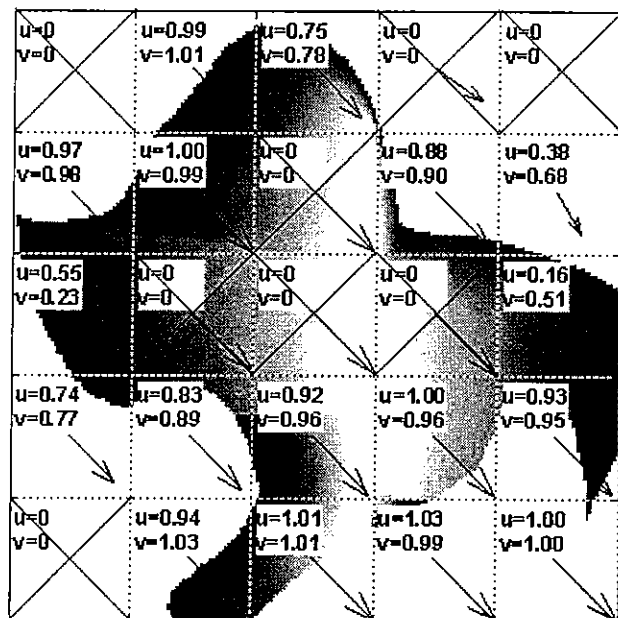
Equations 5.3, 5.7 and 5.8 are the modifications to the image flow algorithm that allow exclusion of most of the velocity results that do not fit the criteria in Equation (5.2) due to limitations in the image flow algorithm. Sample results of application of these modifications are shown in Figures 17, 18 and 19 for the no noise case, the 3% noise case, and 7 % noise case respectively. In all three figures, (a) shows the image flow results prior to modification, (b) shows the image flow results with corrections for little or no contrast, (c) shows the image flow results with corrections for little or no contrast and corrections for gradual intensity gradients, and (d) shows the image flow results with corrections for little or no contrast, corrections for gradual gravity gradients, and corrections for parallel feature orientation. The modifications exclude velocities in the cells that do not fall within the Equation (5.2) criteria. If the velocities found at different points on the synthetic object are averaged to obtain a velocity for the entire object, the average component velocities are within 2% of the expected values ( $u=1, v=1$ ) for the noise free case, within 4% of the expected values for the 3% noise case, and within 9% of the expected values for the 7% noise case.



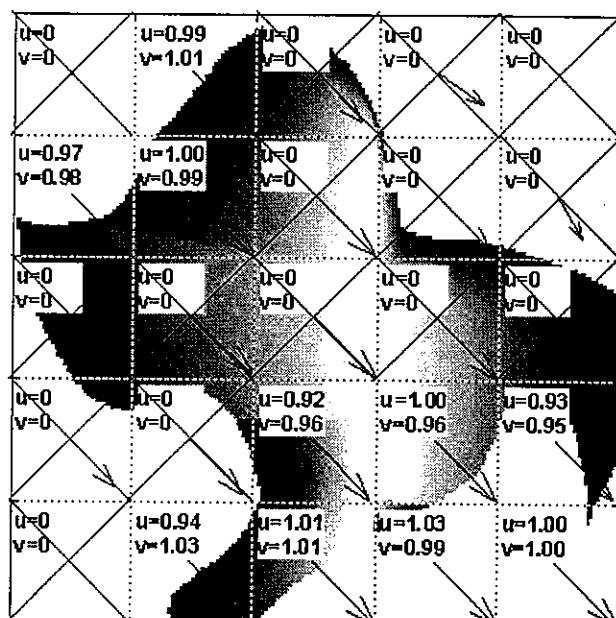
a. No Modifications Applied: No Noise Added - 5x5 Grid



b. Modification 1 Applied: No Noise Added - 5x5 Grid

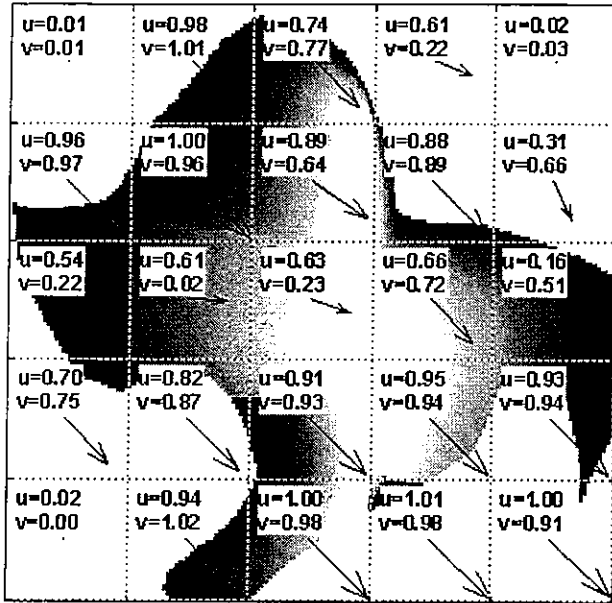


c. Modifications 1 and 2 Applied: No Noise Added - 5x5 Grid

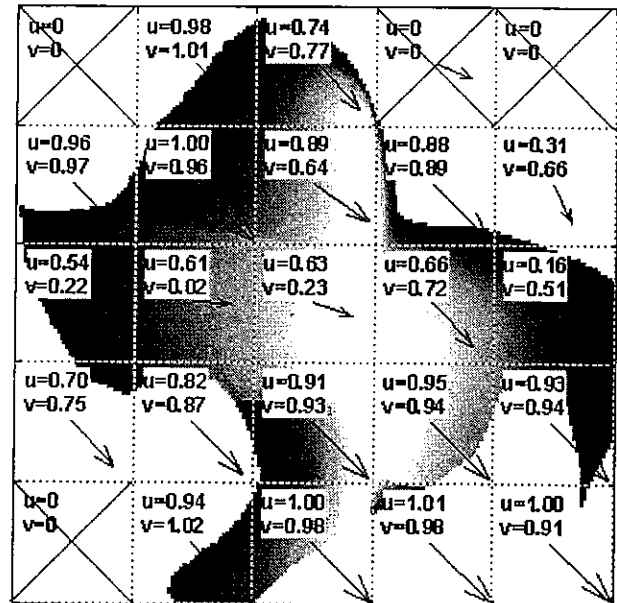


d. Modifications 1, 2 and 3 Applied: No Noise Added - 5x5 Grid

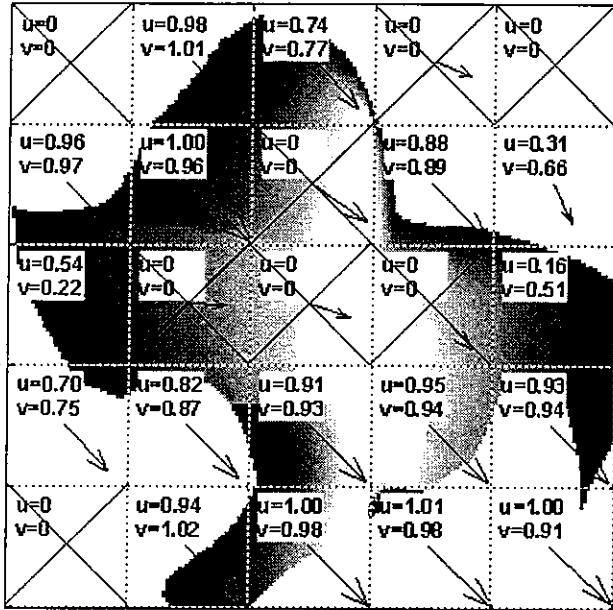
Figure 17. No Noise Added: Results of Modifications



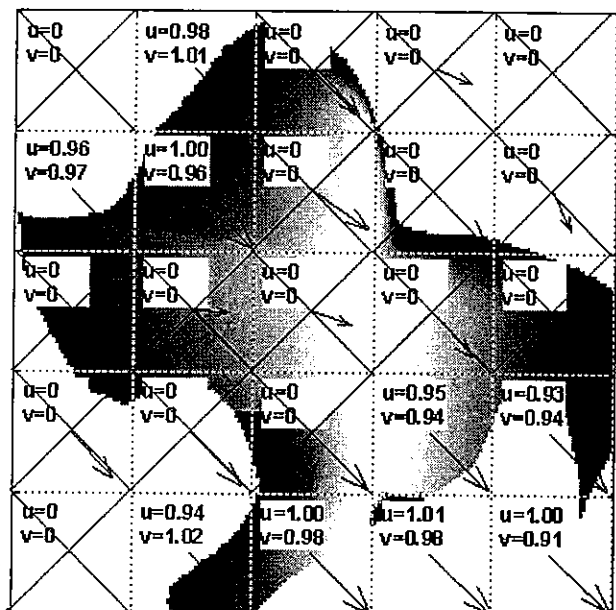
a. No Modifications Applied: 3% Noise Added - 5x5 Grid



b. Modification 1 Applied: 3% Noise Added - 5x5 Grid

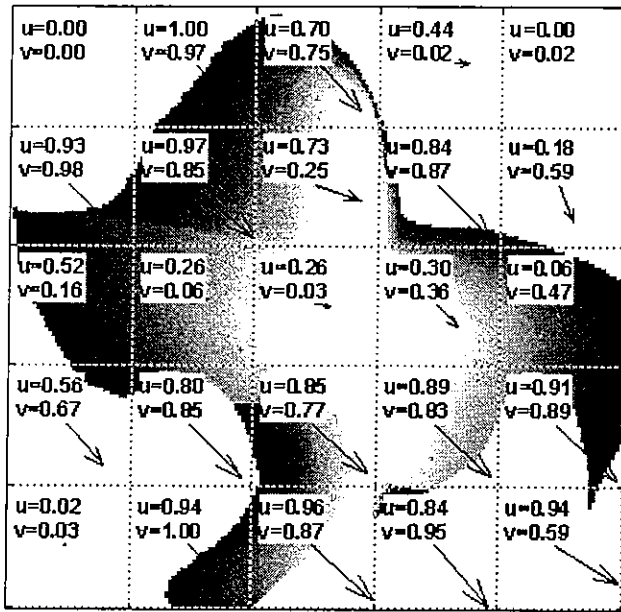


c. Modifications 1 and 2 Applied: 3% Noise Added - 5x5 Grid

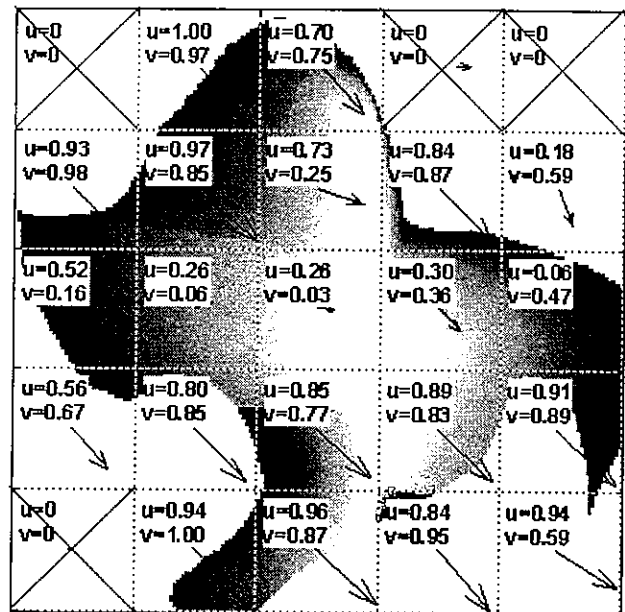


d. Modifications 1, 2 and 3 Applied: 3% Noise Added - 5x5 Grid

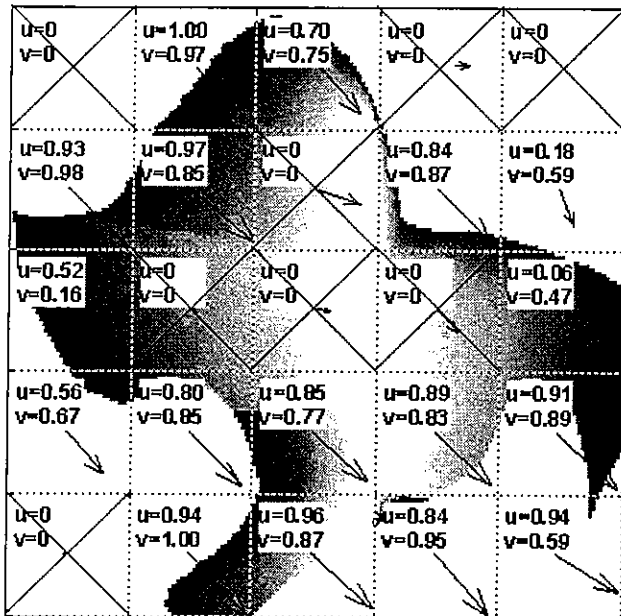
Figure 18. 3% Noise Added: Results of Modifications



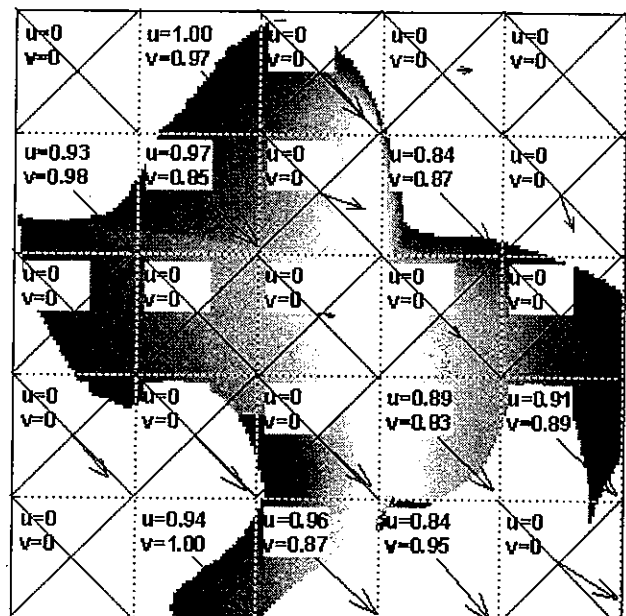
a. No Modifications Applied: 7% Noise Added - 5x5 Grid



b. Modification 1 Applied: 7% Noise Added - 5x5 Grid



c. Modifications 1 and 2 Applied: 7% Noise Added - 5x5 Grid



d. Modifications 1, 2 and 3 Applied: 7% Noise Added - 5x5 Grid

Figure 19. 7% Noise Added: Results of Modifications

## **5.2. Image Flow Applied to the PASDE**

### **5.2.1. PASDE Digitized Image Sequence Description**

A digitized image sequence from the PASDE was chosen to illustrate the ability of the image flow algorithm to measure solar array motion. The image sequence used is from the PRCS Test #3, Firing #3, Tip 6 camera. This sequence provides both north-south and east-west (as observed in the image plane) oscillatory motion of the Kvant-II solar array. See Figure 20 for the first frame of the PASDE digitized image sequence.

### **5.2.2. Grid Specification and Analysis Preliminaries**

The maximum framewise motion is less than 0.6 pixels in either component direction. Therefore, the simple estimates for partial derivatives of intensity ( $I_x$ ,  $I_y$ , and  $I_t$ ) in Equation (4.11) were used.

A 7x10 analysis grid was chosen and provides 70 analysis points on the solar array to demonstrate that several points on the structure can be analyzed at once. This grid was chosen so that each of the subimages of the grid contains a portion of the solar array. Subimage size for this case was 45x45 pixels. Each subimage was subsequently broken into a smaller 5x5 subgrid of 9x9 subimages for calculation of image plane velocities. This results in 25 image plane velocities calculated for each 45x45 subimage that were averaged to find the total velocity measurement for the subimage. Figure 20 shows the analysis grid. Although time histories were found for all seventy locations, nine locations (marked by numbers 1-9) were chosen in different locations on the solar array to provide a sample output. The 9 sample outputs represent portions of the solar array with varying contrast features.

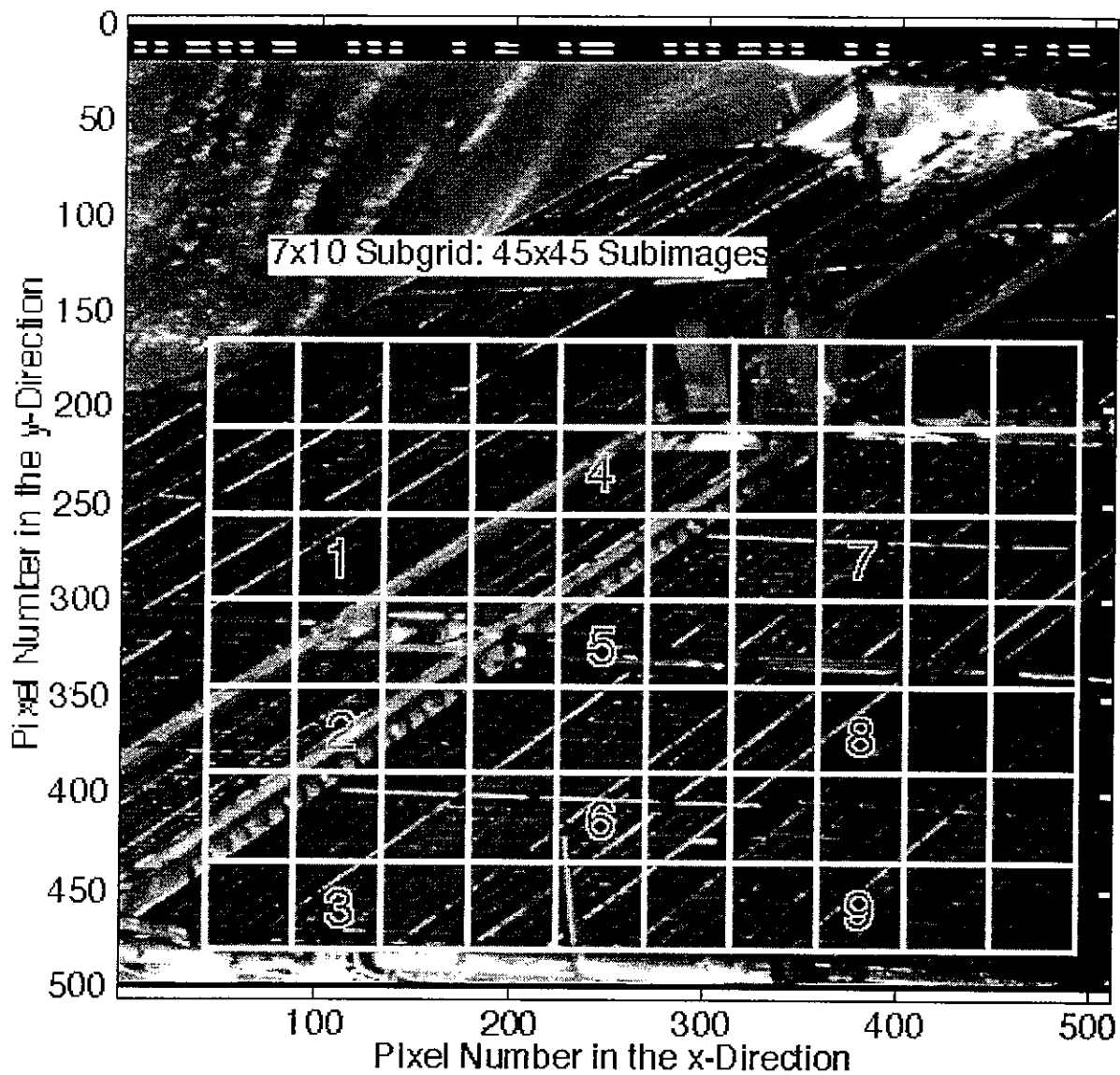
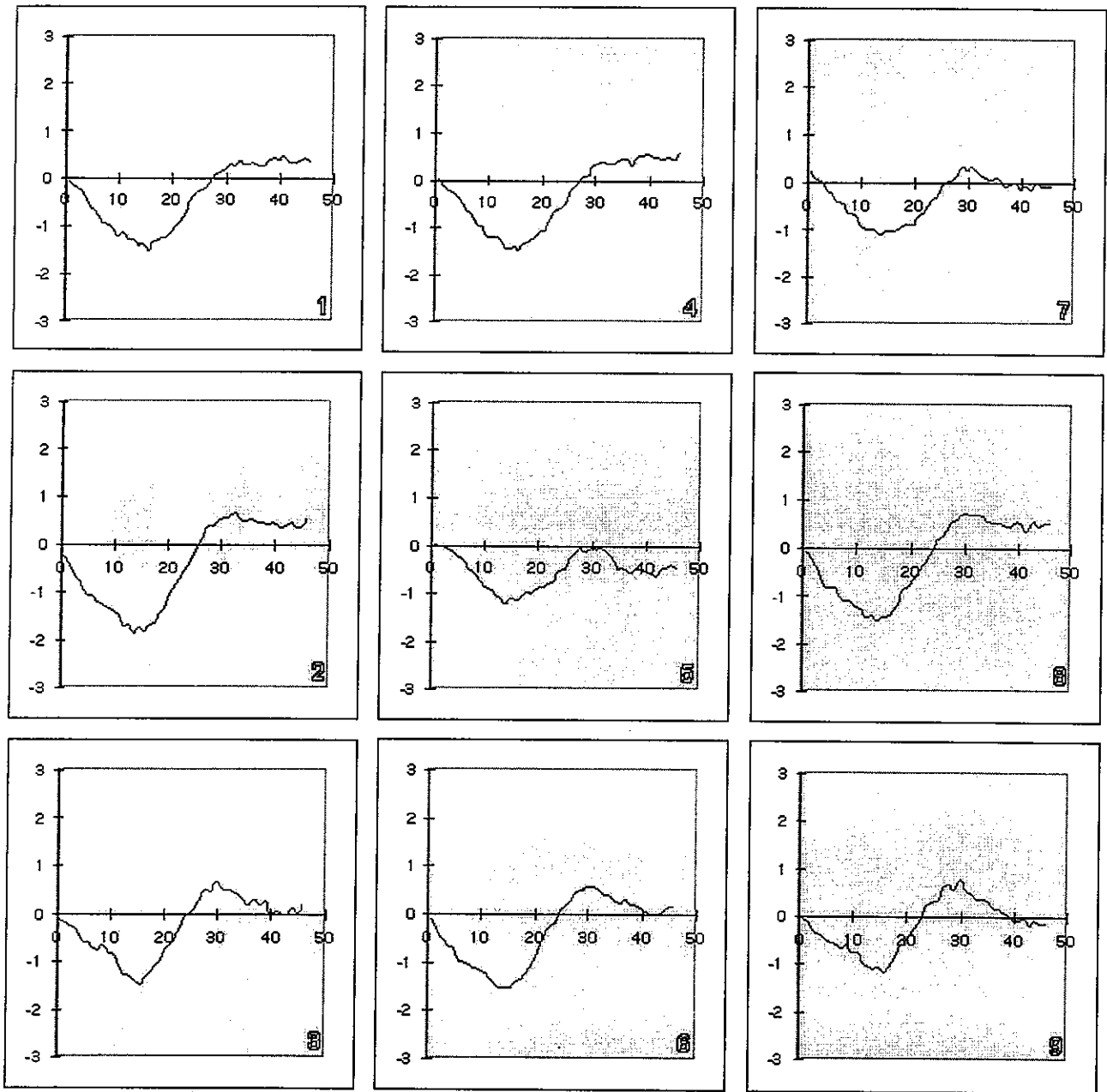


Figure 20. First Frame of the PASDE Camera Sequence with the Analysis Grid

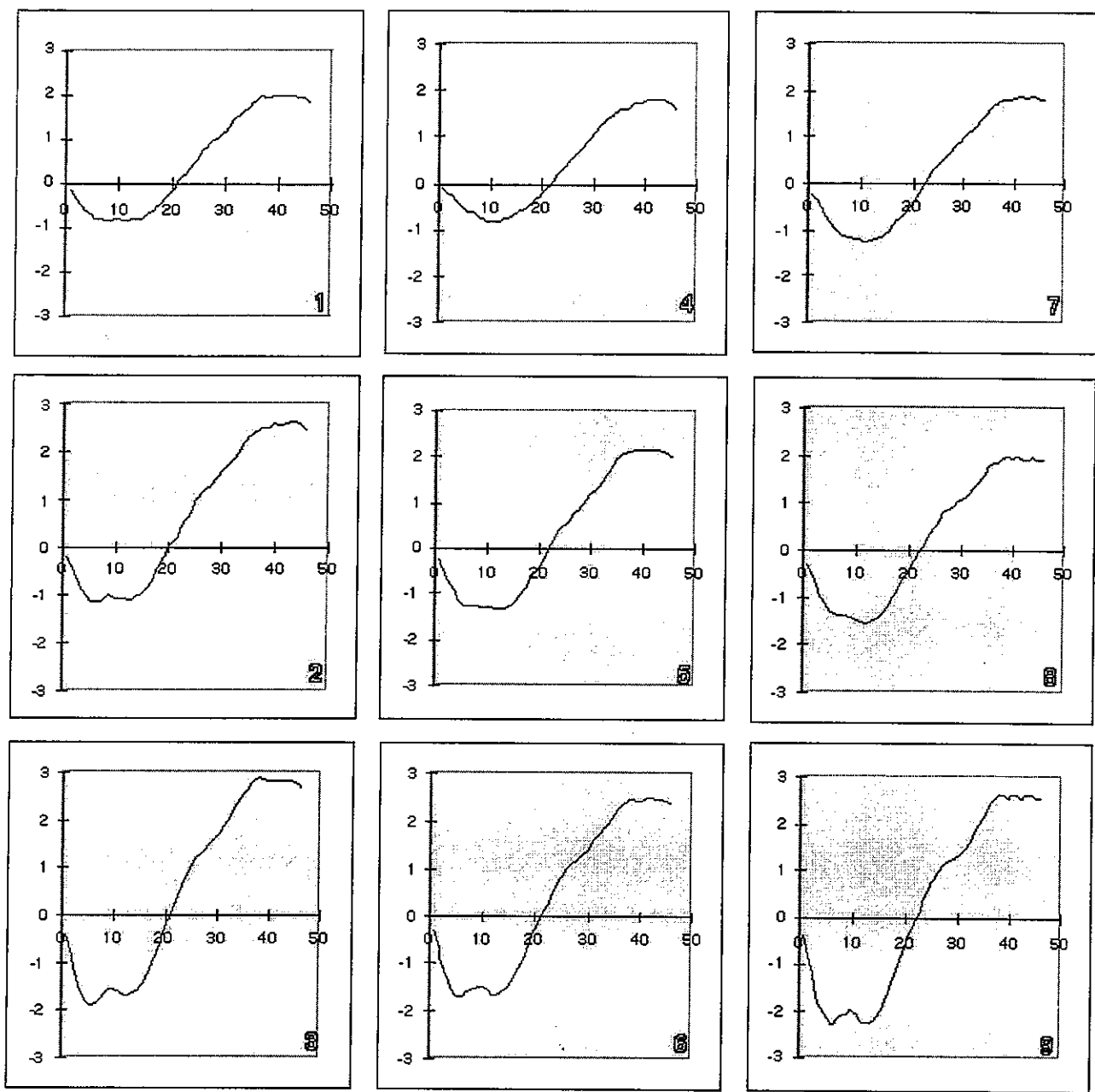
Sample time histories for the x-direction and y-direction motion are shown in Figures 21 and 22, respectively. These displacement time histories are numbered to match the subimage locations in Figure 20 and have been converted from the velocity results obtained by the image flow algorithm. Forty-seven frames at ten frames per second or almost five seconds of data are shown. The out-of-plane solar array bending motion of the solar array is seen as primarily y-direction motion in the image sequence chosen. Notice that the time histories in the y-direction in Figure 22 have a smaller amplitude near the root of the array (locations 1, 4, and 7) than near the tip of the array (locations 3, 6, and 9). In the y-direction, the array acts as a cantilevered plate so the motion of the array is expected to be greater than the motion at the root of the array. Motion in the x-direction is primarily in-plane bending of the array. The array has more stiffness in the x-direction so the motion near the tip of the array is not expected to be significantly larger than the motion near the root of the array as seen in the time histories in Figure 21.

Motions at the root of the solar array are due to the motion of the Mir space station relative to the docked Shuttle. The Mir/Shuttle motions vary with the excitation event. Mir/Shuttle system motions and Kvant II solar array motions are both detected using photogrammetric measurement.



X-axis = Time (frames)  
 Y-axis = Displacement (pixels)

Figure 21. X-Direction Time Histories of the Kvant-II Solar Array



X-axis = Time (frames)  
 Y-axis = Displacement (pixels)

Figure 22. Y-Direction Time Histories of the Kvant-II Solar Array

### **5.2.3. Comparison of Image Flow to Local Feature Tracking Methods**

The image flow algorithm should be comparable in performance to the local feature tracking algorithms of line tracking and scene correlation. Line tracking and scene correlation perform similarly and are compared in Gilbert et al., [1997]. Therefore, image flow was compared only to scene correlation. The 45x45 subimage shown in Figure 23 was used as the comparison image. This subimage is directly to the right of subimage 6 in Figure 20.

To compare image flow velocities to displacements, the framewise velocities were multiplied by the time increment between frames to obtain image plane framewise displacements. Figure 24 shows 20 frames or 2 seconds of cumulative displacement for the scene correlation and the image flow methods in the x and y directions. These time histories represent image flow velocities obtained without applying modifications to the image flow algorithm. The x-direction has a correlation of 0.913 and the y-direction has a correlation of 0.939 between the two methods.

### **5.2.4. Modifications of Image Flow Applied to the PASDE Analysis**

Modification 1 in Equation (5.3) is applied to subimages with little or no change in intensity. Modification 2 in Equation (5.7) is applied to subimages with a gradual change in intensity. Modification 3 in Equation (5.8) is applied to subimages with edges oriented so that they are close to parallel to the direction of the image flow velocity vector. The modifications developed on the test image were applied to the PASDE data in four different combinations. Figure 25 shows the effect of modification 1. This modification provides a slight improvement in correlation to 0.941 and 0.940 in the x and y directions, respectively. Figure 26 shows the effects of modification 1 along with

modification 2. This modification decreases the correlation to 0.889 and 0.934 in the x and y directions, respectively. Therefore, this modification is not necessary in the PASDE analysis. Figure 27 shows the effects of modifications 1, 2, and 3 combined. Even though modification 2 is not applicable, there is a significant improvement in correlation to 0.944 and 0.950 in the x and y directions, respectively. Figure 28 shows the effects of modifications 1 and 3 and excludes modification 2. Exclusion of modification 2 produces the best correlation results of 0.955 in the x-direction and 0.952 in the y-direction because the PASDE data does not have areas with a smooth gradual gradient.

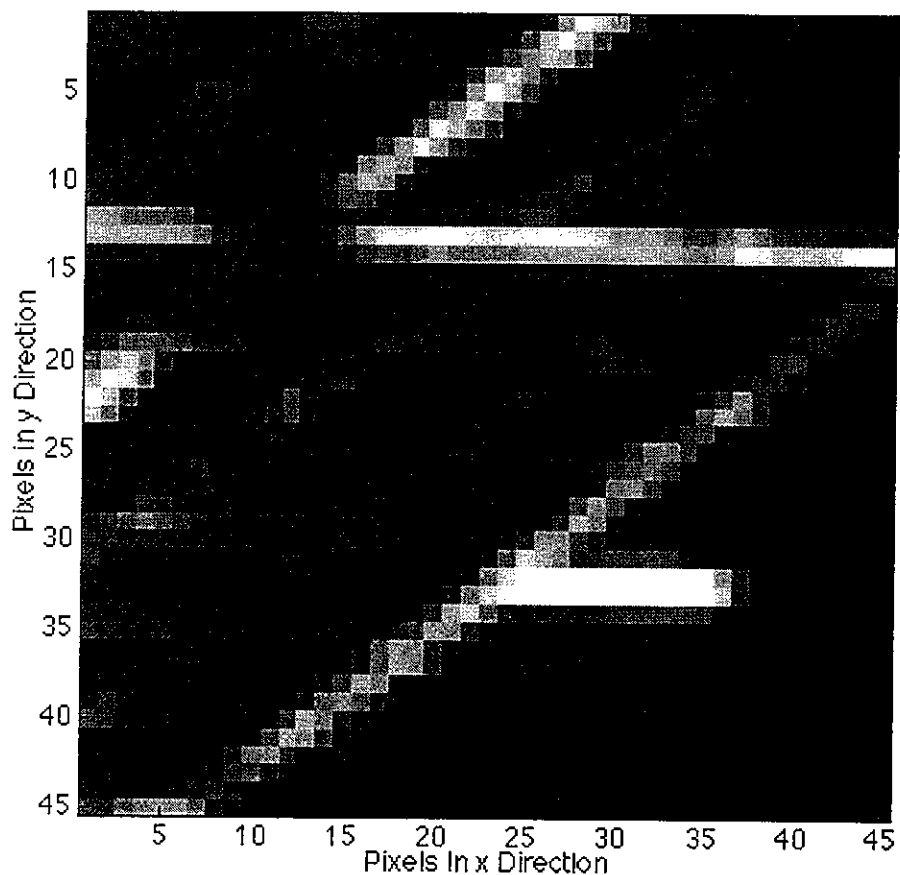


**Figure 23. Image for Comparison of Scene Correlation and Image Flow**

Figures 24 through 28 show graphically that the image flow method performs comparably to the scene correlation method. For a two-frame image sequence, image flow calculations run about an order of magnitude faster than scene correlation calculations for the same subimage area because image flow calculations use addition while scene correlation calculations use multiplication. For one analysis, image flow produces time history results for several subimages at a time while scene correlation produces results for one subimage. For scene correlation, the amount of shift of one subimage over the other must be determined prior to analysis so the method cannot be automated.

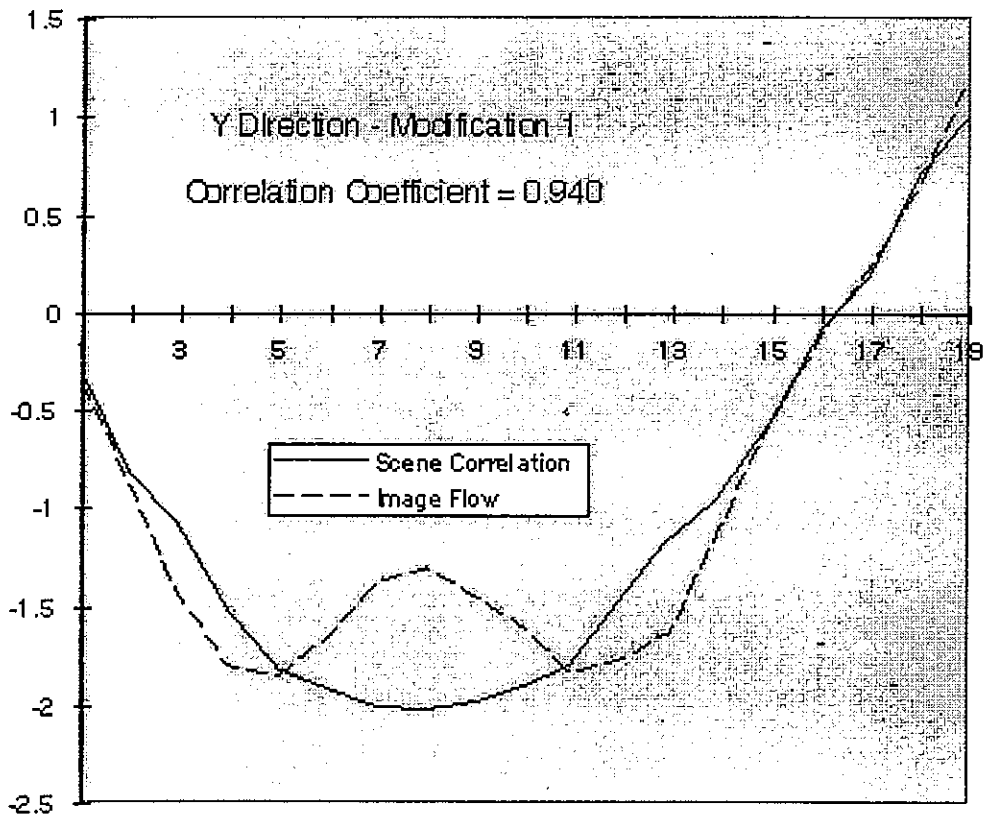
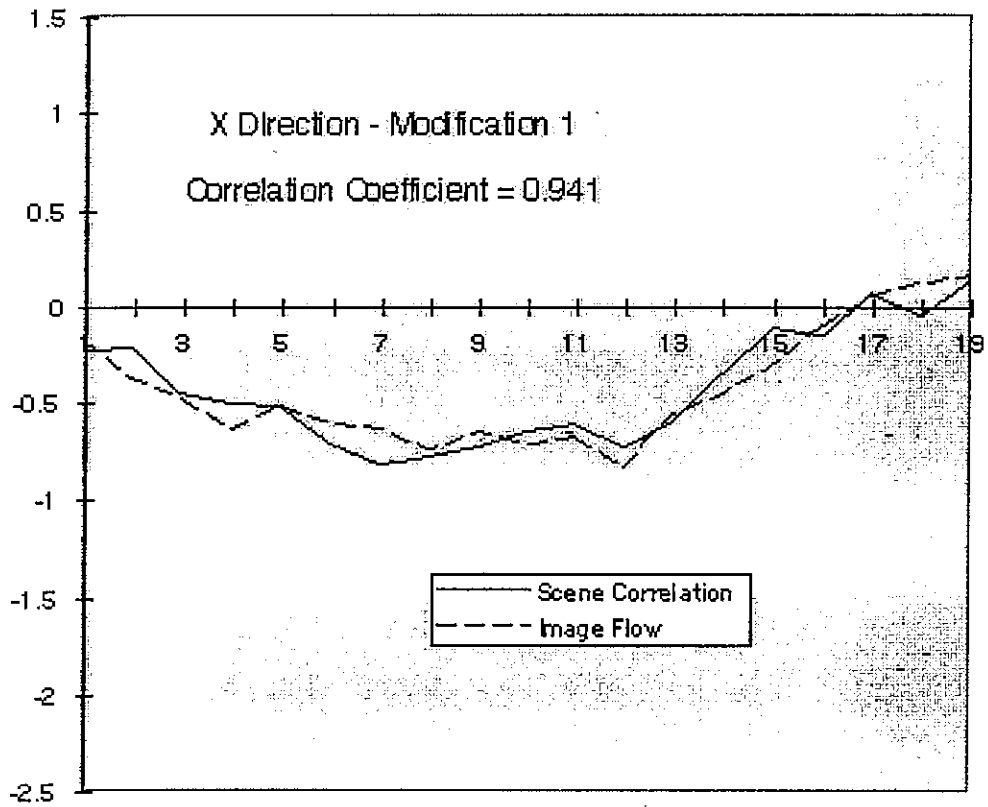


Figure 25. Comparison with Modification 1

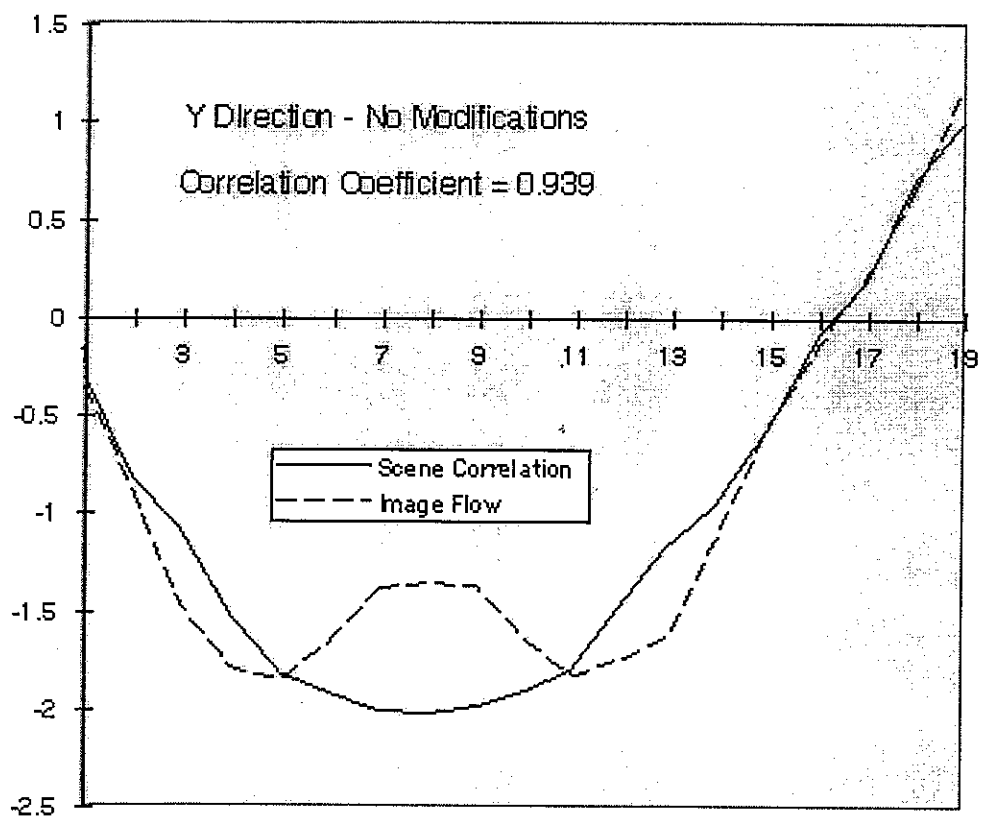
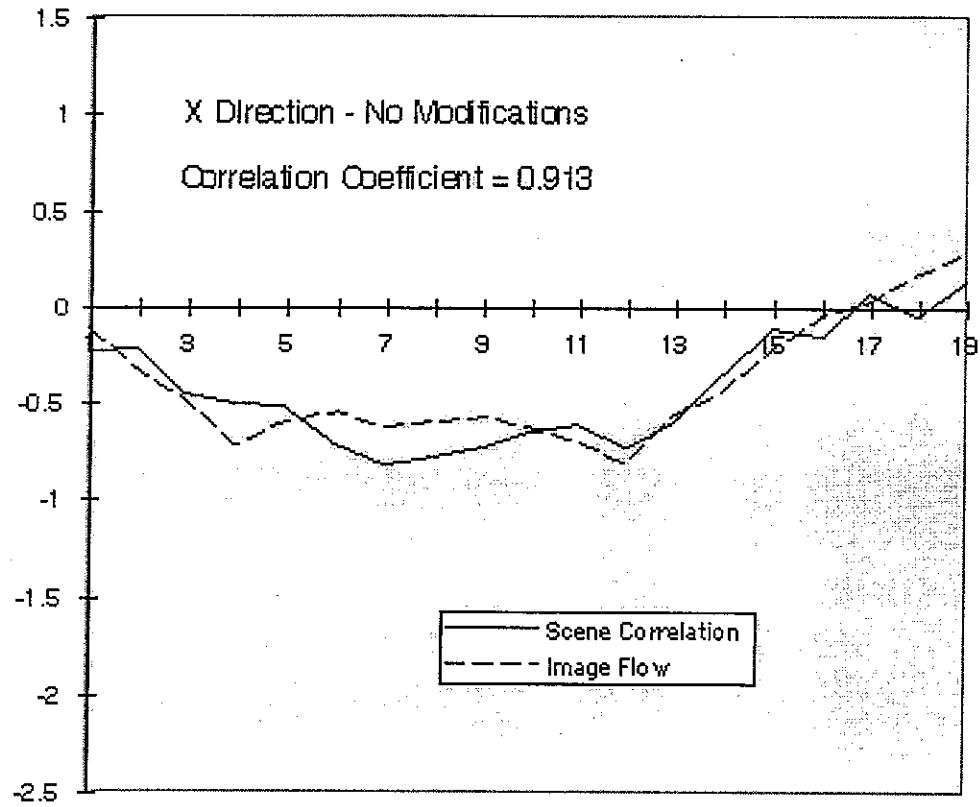


Figure 24. Comparison with no Modifications

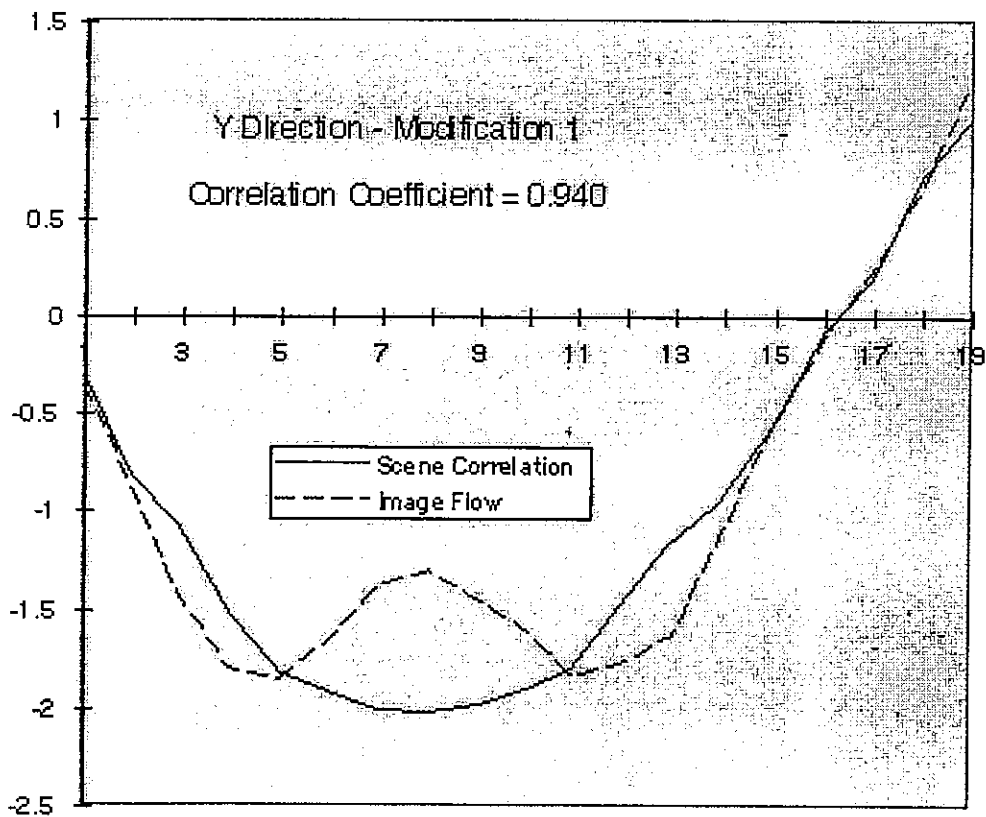
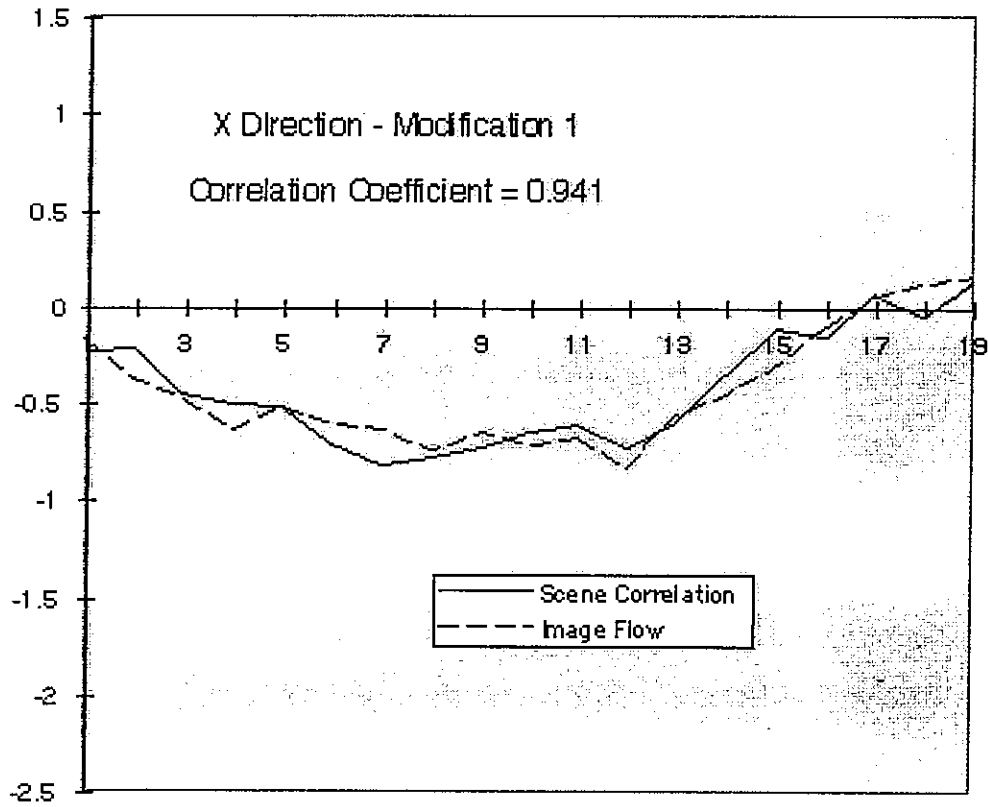


Figure 25. Comparison with Modification 1

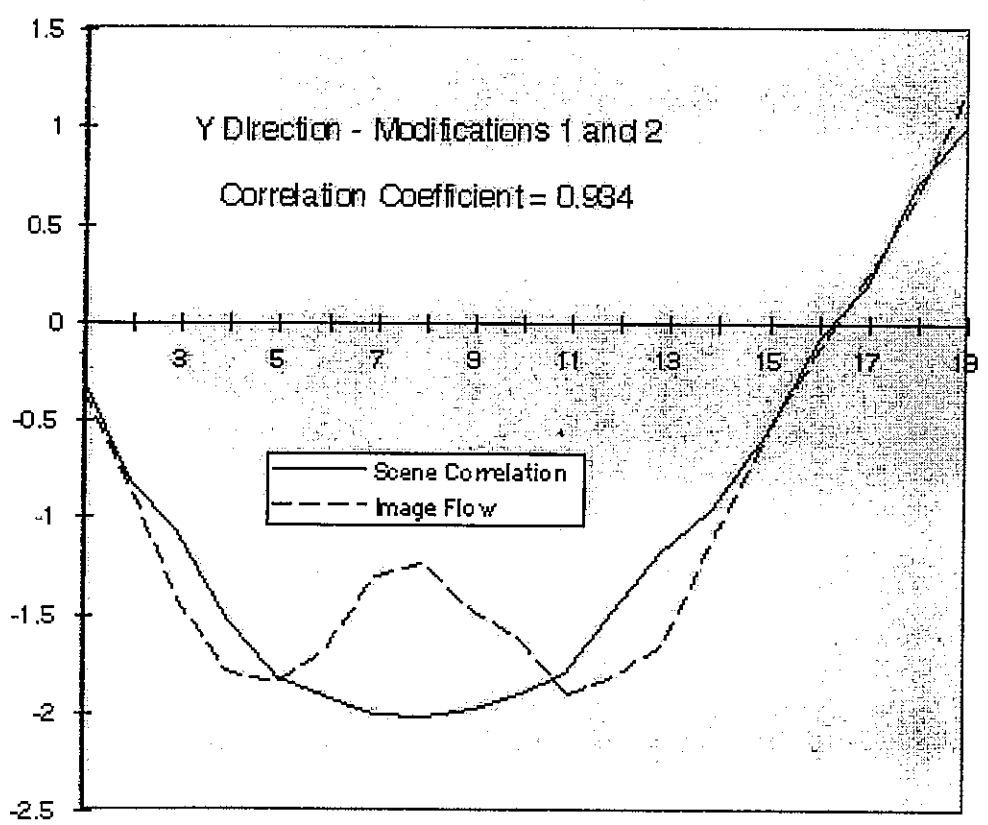
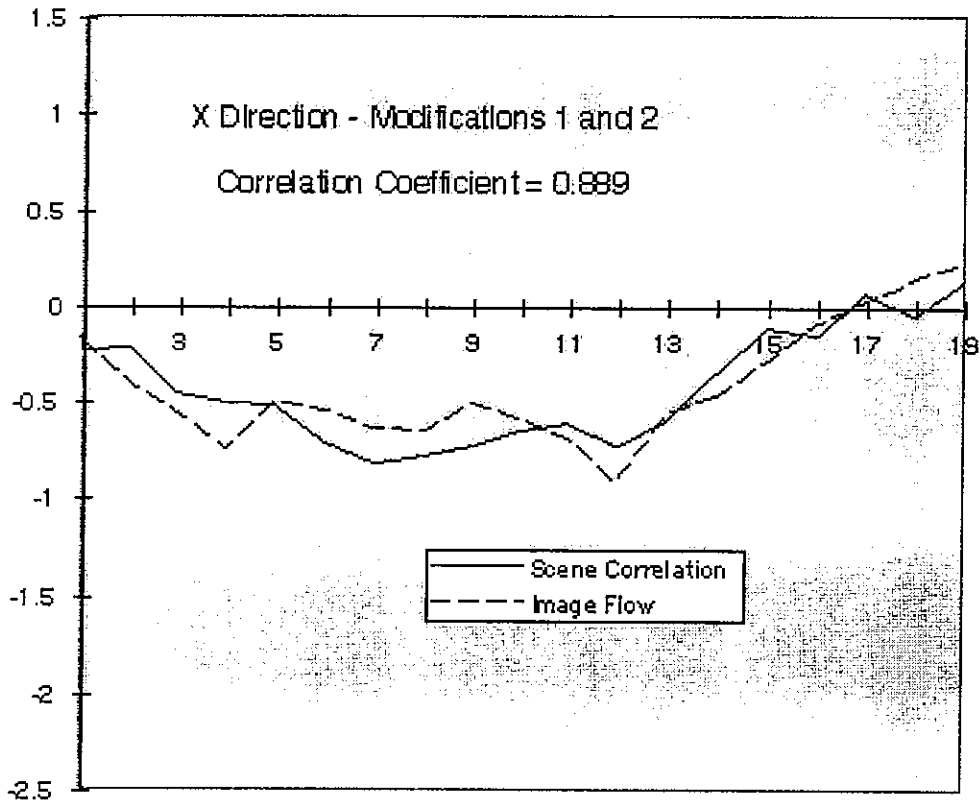


Figure 26. Comparison with Modifications 1 and 2

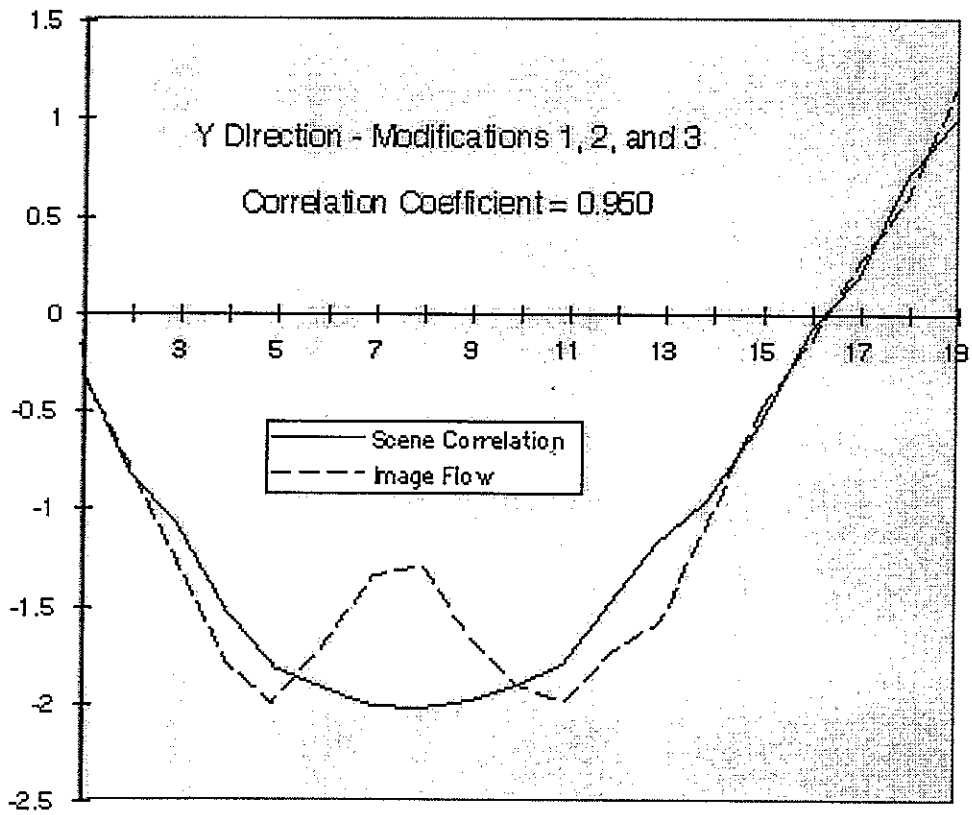
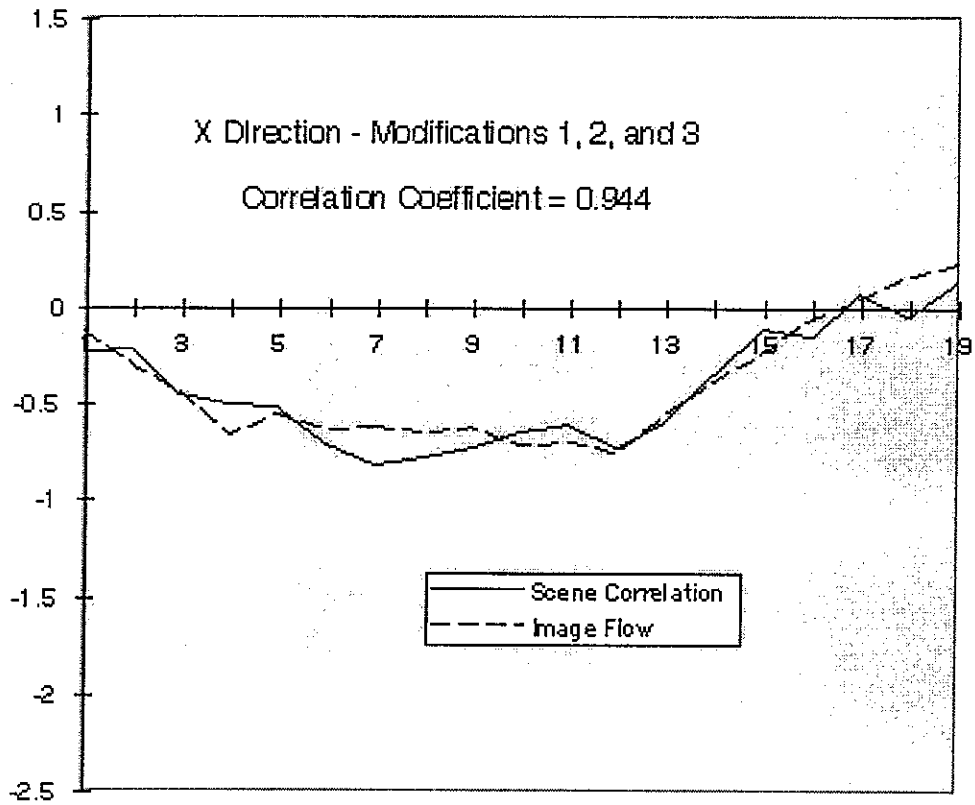


Figure 27. Comparison with Modifications 1, 2, and 3

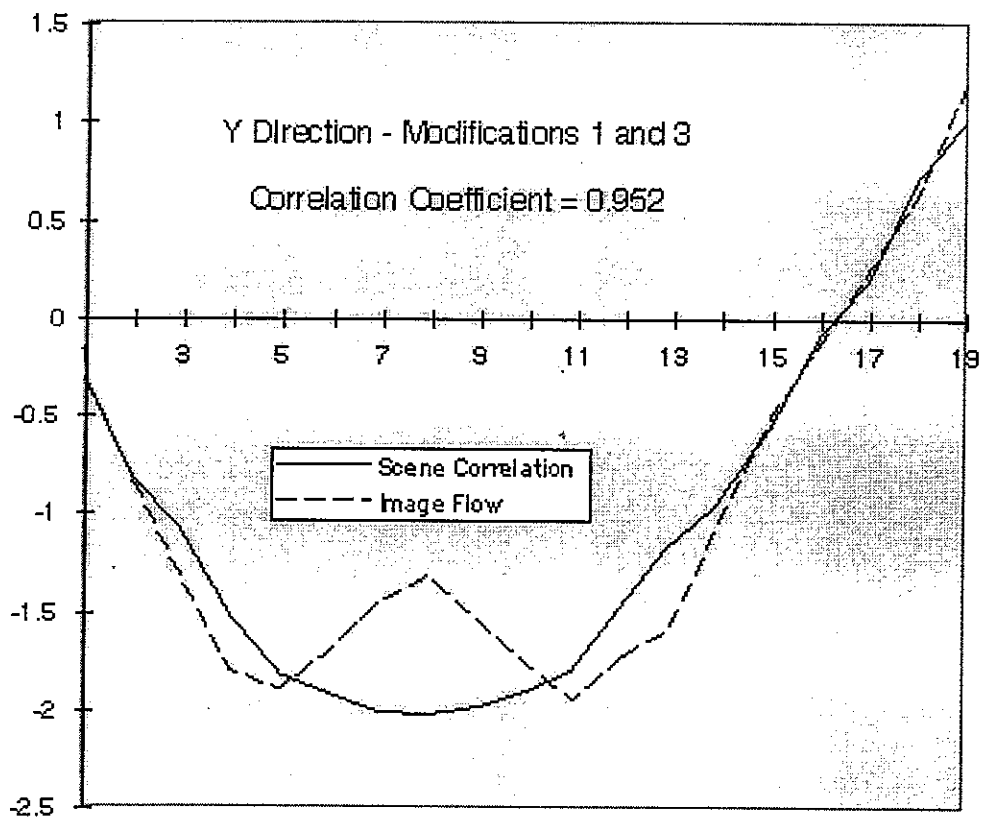
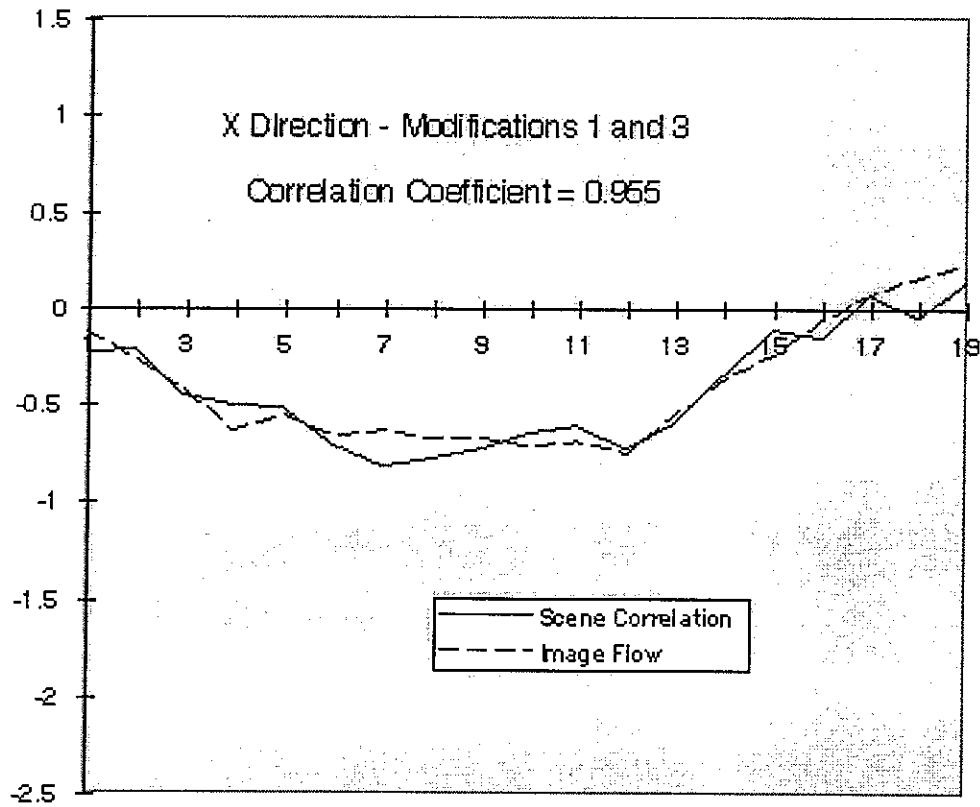


Figure 28. Comparison with Modifications 1 and 3

## 6. Conclusions

The global grid image plane tracking algorithm, image flow, was developed for use with photogrammetric methods of measuring space station appendage vibration. Image flow was tested on synthetic image data first to determine constraints, limitations, and to develop modifications to deal with the limitations. The algorithm was then applied to video image data from the PASDE and compared to other methods of image plane tracking.

Image flow results are comparable to results from local feature tracking methods and therefore may be used in ISS applications. The major advantage of using image flow on ISS photogrammetric measurement is that feature selection for tracking is autonomous. Image flow eliminates the need for selection of high contrast features prior to analysis by extracting measurements on a global grid basis. A convenient grid may be chosen without looking at the image prior to analysis and overlaid on any part of the image. Image flow calculates time histories for several points on the structure at one time rather than tracking one feature at a time. Image flow averages measurements over an entire subimage region, so it is possible to reduce local noises experienced by feature tracking methods. Image flow also provides several measurement points in the amount of time scene correlation takes to obtain one measurement point.

The modifications to correct inaccurate calculations of velocity are experiment dependent in this study. However, further experimentation in future studies would produce modifications that may be determined for a group of image studies such as similar targeted arrays on the ISS that have similar image intensity patterns.

## References

- Gilbert, M.G. and Welch, S.S., "STS-74/Mir Photogrammetric Appendage Structural Dynamics Experiment," *NASA TM 110249*, April 1996.
- Gilbert, M.G.; Welch, S.S.; Pappa, R.S.; Demeo, M.E., "STS-74/Mir Photogrammetric Appendage Structural Dynamics Experiment Preliminary Data Analysis," *NASA TM 110324*, February 1997.
- Holmes, G.R., "Image Plane Modal Identification in Photogrammetric Dynamic Analysis," Master's Thesis, The George Washington University, November 1995.
- Horn, B.K.P. and Schunck, B.G., "Determining Optical Flow," *Artificial Intelligence*, Vol. 17, 1981, pp. 185-203.
- Hornbeck, R.W., *Numerical Methods*, Prentice-Hall, Inc., Englewood Cliffs, New Jersey, 1975.
- Juang, J.-N., *Applied System Identification*, Prentice-Hall, Inc., Englewood Cliffs, New Jersey, 1994.
- Kaplan, M.H., *Modern Spacecraft Dynamics and Control*, John Wiley and Sons, Inc., New York, New York, 1976.
- Moffitt, F.H., *Photogrammetry*, Second Edition, International Textbook Company, Scranton, Pennsylvania, 1967.
- Pappa, R.S., Gilbert, M.G., Welch, S.S., "Simulation of the Photogrammetric Appendage Structural Dynamics Experiment," *NASA TM 110221*, November 1995.
- Rektorys, *Survey of Applicable Mathematics*, Revised Edition, Iliffe, London, England, 1969.
- Shames, I.H., Dym, C.L., *Energy and Finite Element Methods in Structural Mechanics*, McGraw-Hill, New York, New York, 1985.
- Welch, S.S., "Design and Performance of an Optical Measurement System for Position Measurement and Control in a Large Gap Magnetic Suspension System," *Videometrics III*, SPIE Vol. 2350, 1994, pp. 115-126.

## A. The Smoothness Constraint of Horn and Schunck

### A.1. Derivation of the Smoothness Constraint

#### A.1.1. Definition

To use the smoothness constraint of Horn and Schunck, the velocities of neighboring points on an object are assumed to be moving with the same general direction and magnitude. If this is true, the flow is expected to be smooth or similar over an entire intensity pattern. The image flow velocity gradients with respect to the image plane coordinates  $(x,y)$  are

$$\left\langle \frac{\partial u}{\partial x}, \frac{\partial u}{\partial y} \right\rangle \text{ and } \left\langle \frac{\partial v}{\partial x}, \frac{\partial v}{\partial y} \right\rangle, \quad (\text{A.1})$$

with magnitudes

$$\sqrt{\left(\frac{\partial u}{\partial x}\right)^2 + \left(\frac{\partial u}{\partial y}\right)^2} \text{ and } \sqrt{\left(\frac{\partial v}{\partial x}\right)^2 + \left(\frac{\partial v}{\partial y}\right)^2}. \quad (\text{A.2})$$

The smoothness constraint is expressed in terms of sum of the squares of the magnitudes [Horn et al., 1981].

$$\left(\frac{\partial u}{\partial x}\right)^2 + \left(\frac{\partial u}{\partial y}\right)^2 + \left(\frac{\partial v}{\partial x}\right)^2 + \left(\frac{\partial v}{\partial y}\right)^2 \quad (\text{A.3})$$

#### A.1.2. The Smoothness Constraint Applied to Image Flow

The image flow problem is solved using an error minimization

$$E_a^2 = (I_x u + I_y v + I_t)^2, \quad (\text{A.4})$$

$$E_b^2 = \left(\frac{\partial u}{\partial x}\right)^2 + \left(\frac{\partial u}{\partial y}\right)^2 + \left(\frac{\partial v}{\partial x}\right)^2 + \left(\frac{\partial v}{\partial y}\right)^2, \quad (\text{A.5})$$

$$E^2 = \iint_{\Omega} (\alpha^2 E_b + E_a) dx dy \quad (\text{A.6})$$

where  $E_a$  is the error of the image flow equation,  $E_b$  is the departure from smoothness,  $E$  is the total error, and  $\alpha^2$  is a weighting factor chosen to be roughly equal to the expected noise of the estimate  $I_x^2 + I_y^2$ . [Horn, et al., 1981] After substituting Equations (A.4) and (A.5) into Equation (A.6), use variational calculus [Shames, et al., 1985], to minimize

$$E^2 = \iint_{\Omega} F(u, u_x, u_y, v, v_x, v_y, x, y) dx dy = \iint_{\Omega} \left\{ \alpha^2 (u_x^2 + u_y^2 + v_x^2 + v_y^2) + (I_x u + I_y v + I_t)^2 \right\} dx dy. \quad (A.7)$$

Solving Equation (A.7) results in two equations for image flow analysis [Horn, et al., 1981].

$$I_x^2 u + I_x I_y v = \alpha^2 \nabla^2 u - I_x I_t, \quad (A.8)$$

$$I_x I_y u + I_y^2 v = \alpha^2 \nabla^2 v - I_y I_t. \quad (A.9)$$

### A.1.3. Estimation of Partial Derivatives and Laplacians

Estimates of partial derivatives  $I_x$ ,  $I_y$ , and  $I_t$  are derived in Chapter 4 and are calculated by Equation (4.9). Estimate Laplacians  $\nabla^2 u$  and  $\nabla^2 v$  of the image flow components using local averages from Equations (A.11) and (A.12) [Horn, et al., 1981]:

$$\nabla^2 u = \kappa (\bar{u}_{i,j,k} - u_{i,j,k}) \quad \text{and} \quad \nabla^2 v = \kappa (\bar{v}_{i,j,k} - v_{i,j,k}) \quad (A.10)$$

where  $\kappa$  is a proportionality factor equal to 3. The local averages are defined as

$$\bar{u}_{i,j,k} = \frac{1}{6} \{ u_{i-1,j,k} + u_{i,j+1,k} + u_{i+1,j,k} + u_{i,j-1,k} \} + \frac{1}{12} \{ u_{i-1,j-1,k} + u_{i-1,j+1,k} + u_{i+1,j+1,k} + u_{i+1,j-1,k} \} \quad (A.11)$$

$$\bar{v}_{i,j,k} = \frac{1}{6} \{ v_{i-1,j,k} + v_{i,j+1,k} + v_{i+1,j,k} + v_{i,j-1,k} \} + \frac{1}{12} \{ v_{i-1,j-1,k} + v_{i-1,j+1,k} + v_{i+1,j+1,k} + v_{i+1,j-1,k} \} \quad (A.12)$$

Using the estimates from Equations (A.11) and (A.12), the image flow equations are rewritten as

$$(\alpha^2 + I_x^2 + I_y^2)(u - \bar{u}) = -I_x(I_x\bar{u} + I_y\bar{v} + I_t), \quad (\text{A.13})$$

$$(\alpha^2 + I_x^2 + I_y^2)(v - \bar{v}) = -I_y(I_x\bar{u} + I_y\bar{v} + I_t). \quad (\text{A.14})$$

#### A.1.4. Iterative Solution

An iterative solution is a computationally less expensive method of solving the above image flow equations than solving the equations simultaneously for  $u$  and  $v$ .

Assuming that the structure is initially at rest for the sequence of images ( $u^0=0, v^0=0$ ) a new set of velocity estimates ( $u^{n+1}, v^{n+1}$ ) are computed from the average velocities of the previous velocity estimates ( $u^n, v^n$ ) [Horn, et al., 1981].

$$u^{n+1} = \bar{u}^n - \frac{I_x [I_x \bar{u}^n + I_y \bar{v}^n + I_t]}{(\alpha^2 + I_x^2 + I_y^2)}, \quad (\text{A.15})$$

$$v^{n+1} = \bar{v}^n - \frac{I_y [I_x \bar{u}^n + I_y \bar{v}^n + I_t]}{(\alpha^2 + I_x^2 + I_y^2)}. \quad (\text{A.16})$$

At the boundaries of the image, some of the points needed to compute the average velocities lie outside the image boundaries. Create a new subimage with a boundary just inside the original so that a buffer zone of pixels is available for this computation.

## ***A.2. Application to the PASDE***

The smoothness constraint was applied to a digitized sequence of PASDE data measured in PRCS Test #3, firing #3. A data sequence from the tip 6 camera starting at MET005/01:57:52 was used to demonstrate the ability of the smoothness constraint to qualitatively assess the direction of object motion. The data sequence is two seconds in length with a frame rate of ten frames per second so the sequence has a total of twenty frames. This sequence was chosen so that during the two seconds of data in the sequence, the Kvant-II solar array goes through a half-cycle of oscillatory motion. In other words, the solar array motion is generally to the north/northwest of the image frame in the first part of the two-second interval and to the south/southeast in the last part of the two-second interval. Disk1 (included with this paper) contains a 1.1 MB animated gif file of this two-second image sequence from PRCS Test #3, Firing #3 that may be viewed with a web browser. An example subimage of high contrast features was chosen from the total image to provide fewer numbers of pixels so that the velocity vectors plotted are easier to view. Figure A1 is the beginning frame of the image sequence used for the study. A box is drawn to designate the smaller subimage chosen. Figure A2 is the expanded detail of the subimage chosen.

The iterative solution in section A.1.4 can be applied two different ways. (1) If the initial estimates of the image plane velocities are chosen as the velocities of the previous frame, only one iteration is required to find the velocities of the current frame. (2) If 5 or more iterations are used, initial velocity estimates for each frame may be set to zero. Six frames (frames 3, 6, 9, 13, 15, and 20) from the twenty frame analysis illustrate the difference in the two methods of applying the iterative solution.

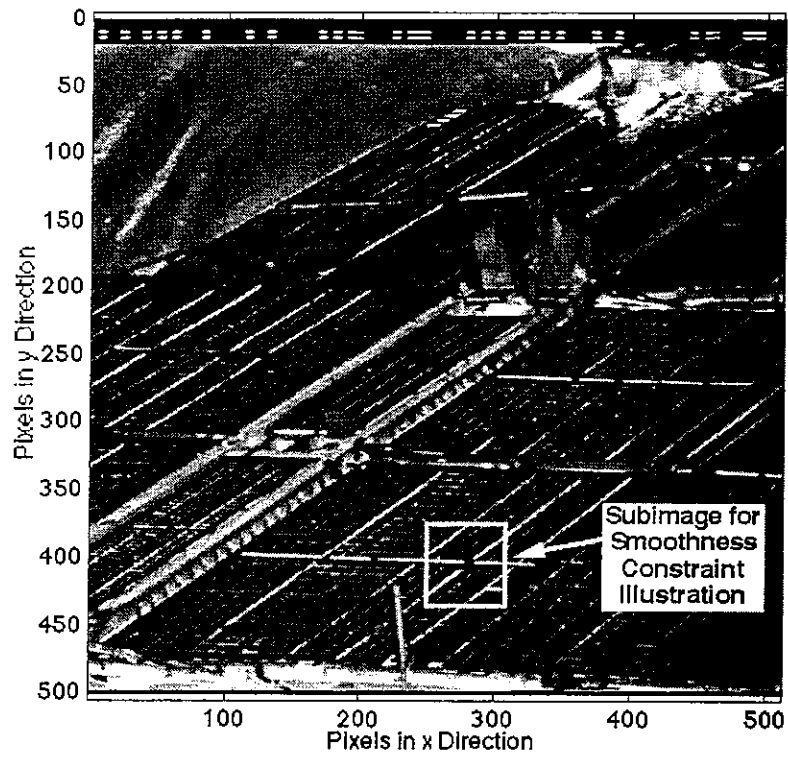


Figure A.1. Start Frame for the Two Second Tip 6 Image Sequence

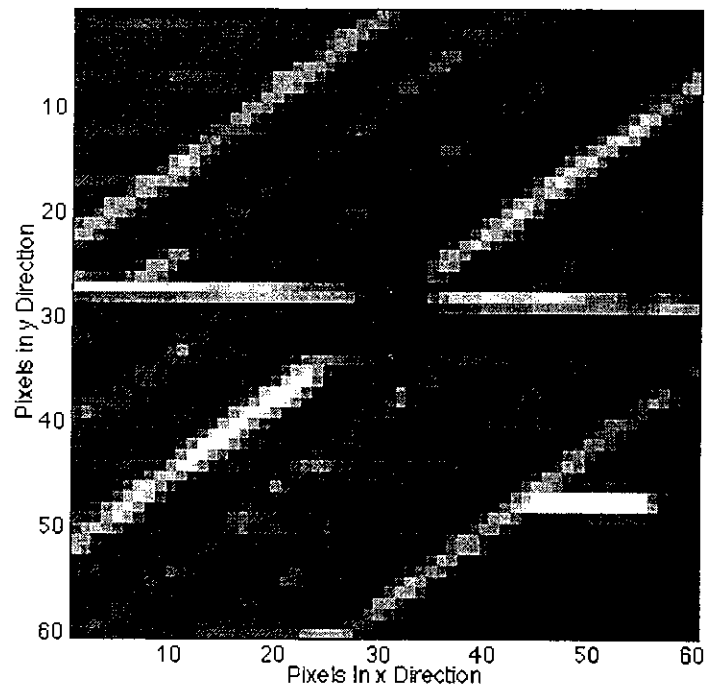


Figure A.2. Expanded Detail of Example Subimage

### **A.2.1. Previous Frame Initial Velocity Estimates with One Iteration**

If the initial velocities of the iterative solution are chosen as equal to the final velocity estimates from the previous frame, only one iteration is required to obtain velocity vectors. If the object continues to move in the same direction through several frames, flow velocities are detected first at high contrast features and then are filled in at areas of low contrast. However, if the object changes direction, high contrast features appear to be going in different directions than the low contrast areas because the velocity estimates lag behind in those areas. Figures A.3 and A.4 show frames 3 and 6, respectively, where the solar array is moving towards north. Figure A.5 shows frame 9, where the solar array is reaching peak displacement and zero velocity. Figures A.6, A.7, and A.8 show frames 13, 15, and 20, respectively, where the solar array is moving towards south. Flow velocities of the high contrast lines are detected first (Figure A.3) and then velocity vectors fill in for the low contrast areas (Figure A.4). Changes in velocity are detected first at the high contrast lines (Figure A.5), while the low contrast estimates lag behind (Figure A.6), change direction (Figure A.7), and fill in to match the direction of motion (Figure A.8). The advantage of this method is low computation time. To get correct sense of velocities, though, the analyst must disregard what is happening in the low contrast areas.

### **A.2.2. Zero Initial Velocity Estimates with Five Iterations**

The more computationally expensive method of increasing the number of iterations and setting the initial velocity estimates to zero highlights the high contrast features only. In this method velocity vectors are obtained only at high contrast features so there is no lag in low contrast areas that the analyst must interpret so the object motion

is clear on first glance. Fortunately, three to five iterations are sufficient to find velocity vectors of the high contrast features. Figures A.9 and A.10 show frames 3 and 6, respectively, where the solar array is moving in an upward direction. Figure A.11 shows frame 9, where the solar array is reaching peak motion and zero velocity. Figures A.12, A.13, and A.14 show frames 13,15, and 20, respectively, where the solar array is moving in a downward direction. This method is very good at showing the velocity decreasing (Figures A.9 and A.10), coming to zero and reversing direction (Figure A.11), and increasing again (Figures A.12, A.13, and A.14).

Both methods of applying the iterative solution stemming from the smoothness constraint show the general trends in motion. However, they cannot be quantified to measure velocities accurately in the image plane. This constraint offers a visual method of determining if the contrast features of the object are sufficient to use image flow. The smoothness constraint of Horn and Schunck was evaluated first as an existing method to determine if it could be used with structural vibrations. However, the smoothness constraint could not be used to quantify image flow velocities so the constant velocity constraint was developed.

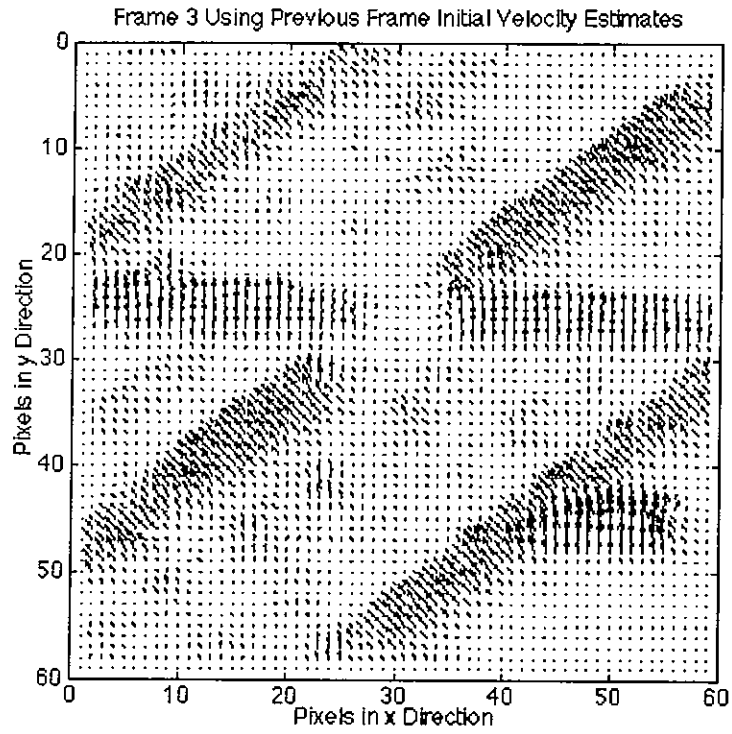


**Figure A.3. Frame 3 of Previous Frame Velocity Estimate Analysis**

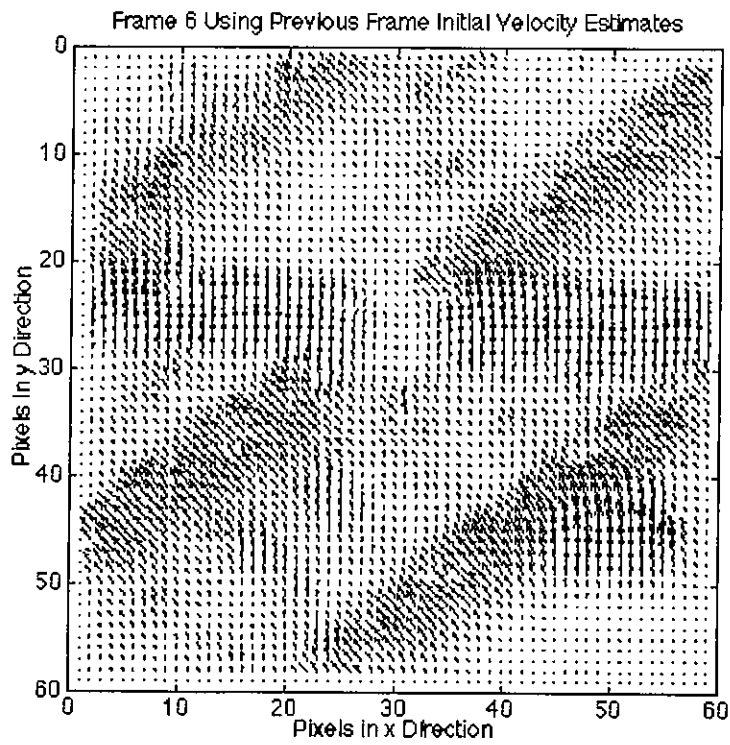


**Figure A.4. Frame 6 of Previous Frame Velocity Estimate Analysis**

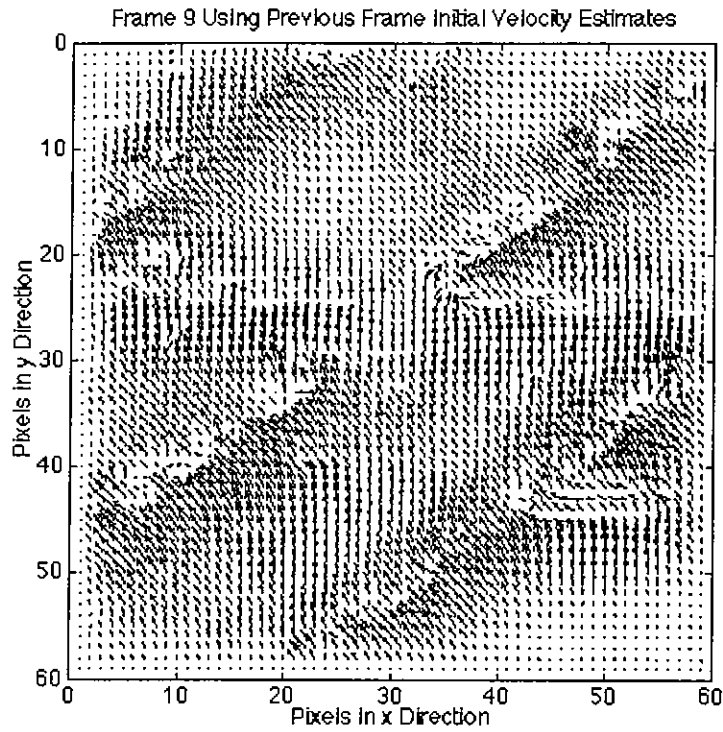


**Figure A.5. Frame 9 of Previous Frame Velocity Estimate Analysis**

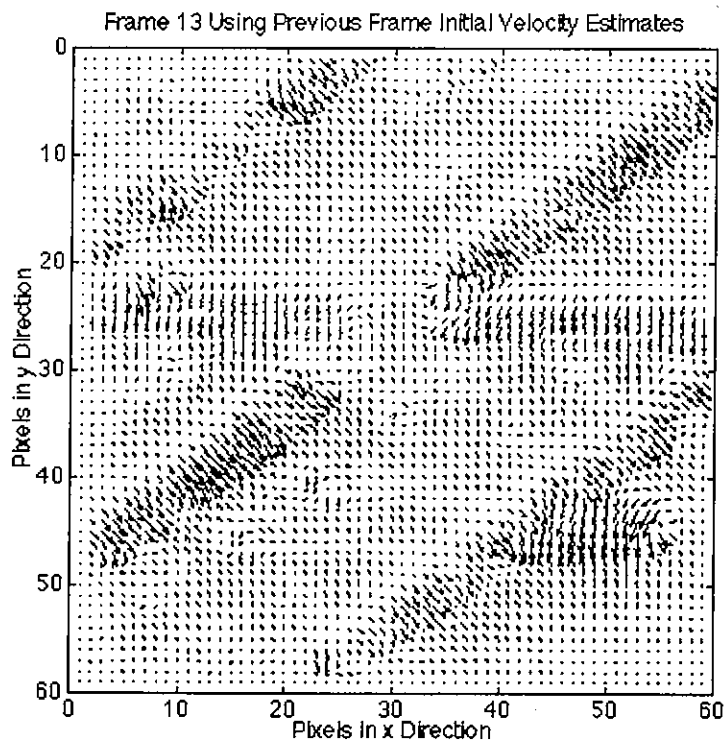


**Figure A.6. Frame 13 of Previous Frame Velocity Estimate Analysis**

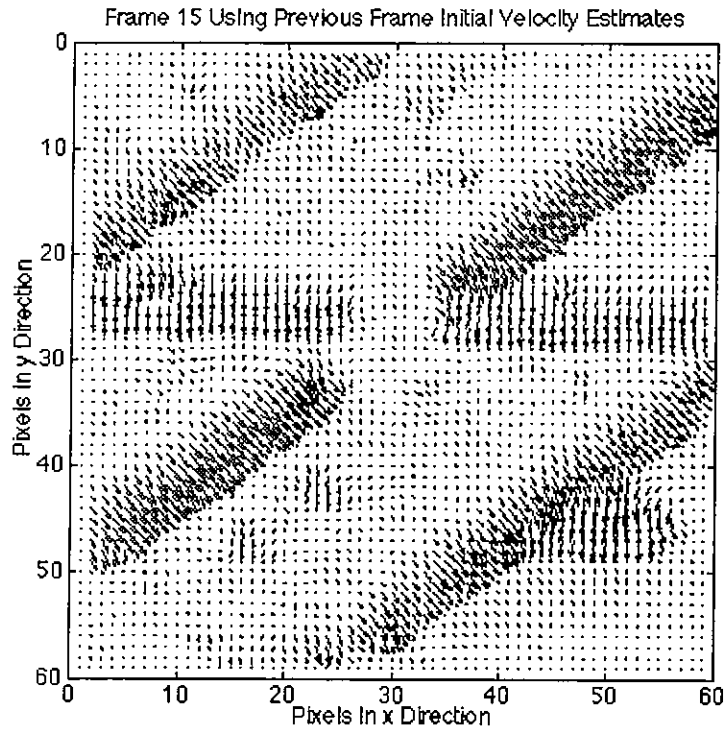


**Figure A.7. Frame 15 of Previous Frame Velocity Estimate Analysis**

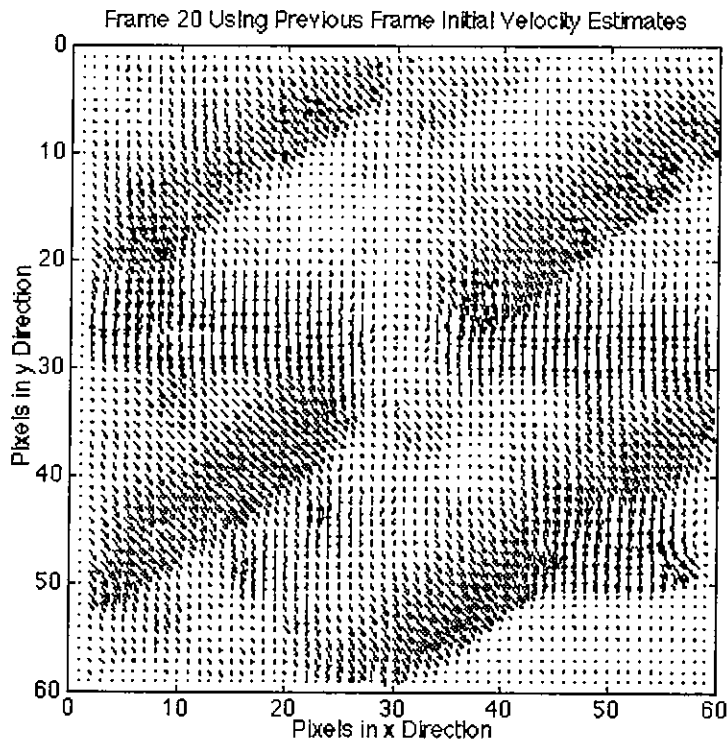


**Figure A.8. Frame 20 of Previous Frame Velocity Estimate Analysis**

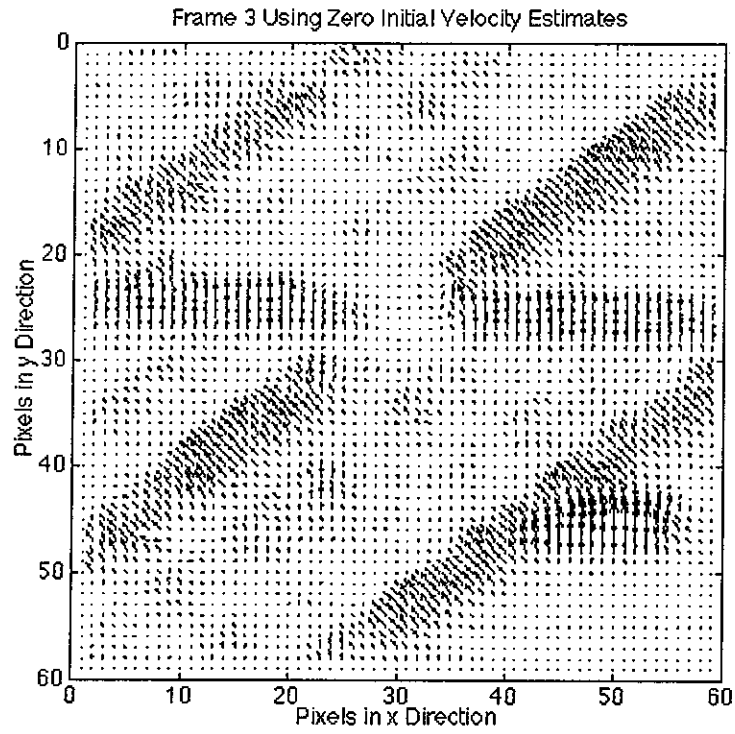


**Figure A.9. Frame 3 of Zero Initial Velocity Estimate Analysis**

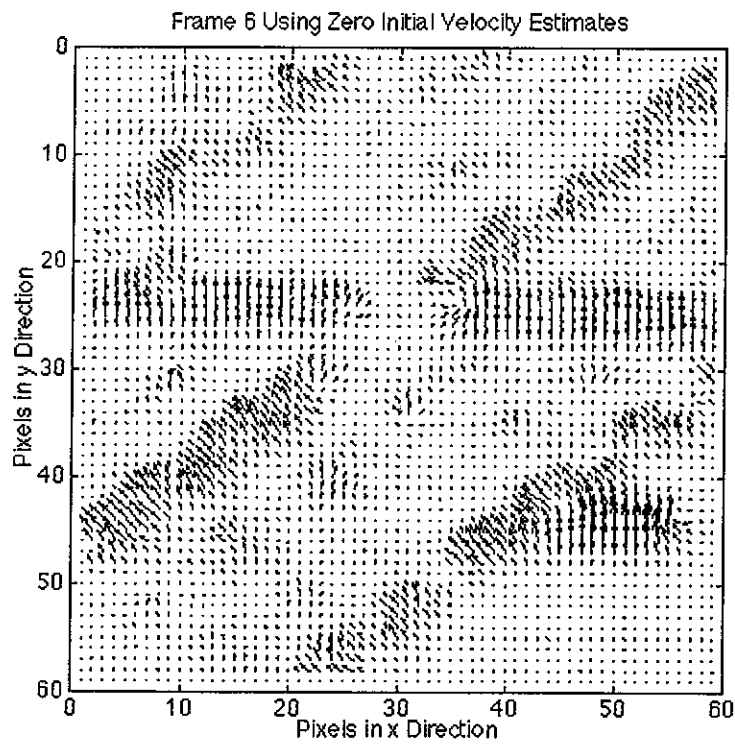


**Figure A.10. Frame 6 of Zero Initial Velocity Estimate Analysis**

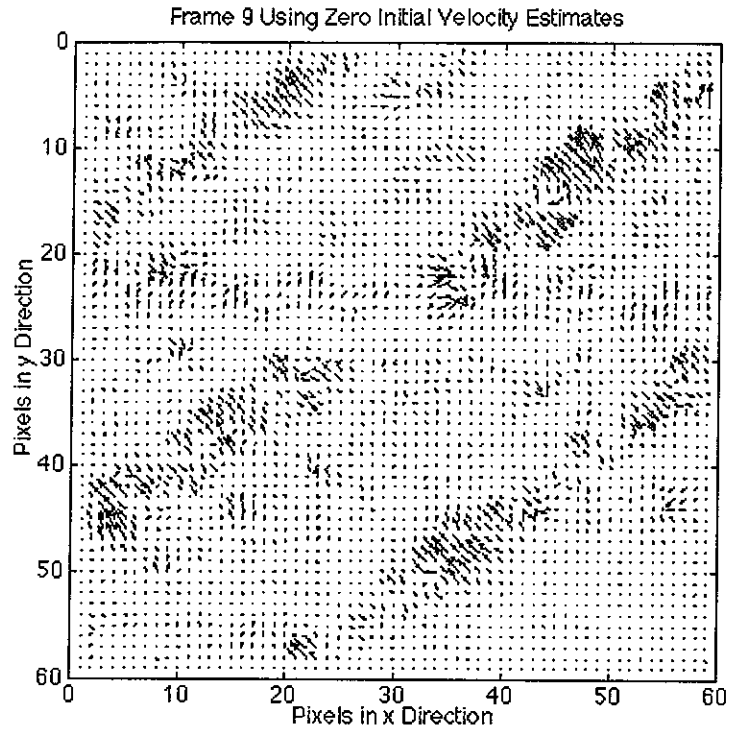


**Figure A.11. Frame 9 of Zero Initial Velocity Estimate Analysis**

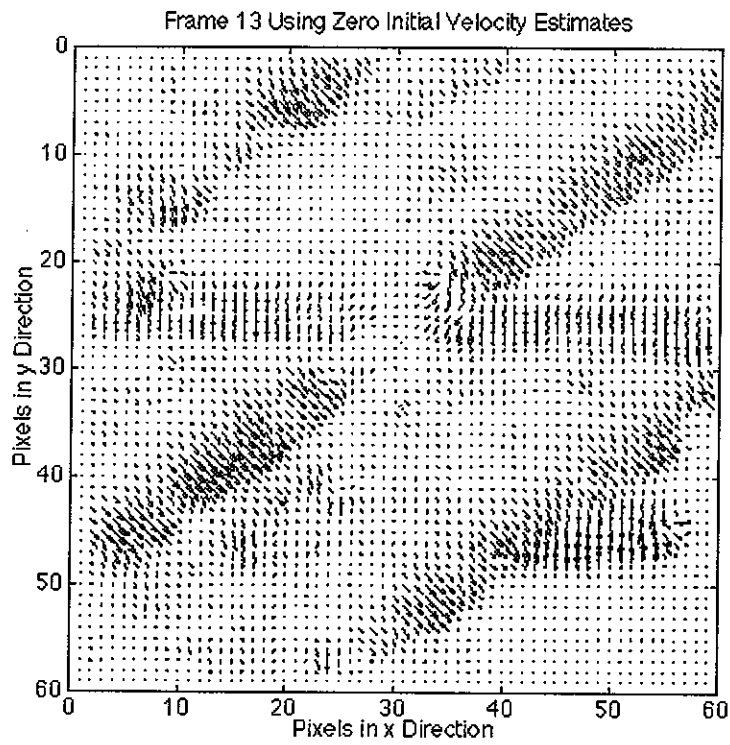


**Figure A.12. Frame 13 of Zero Initial Velocity Estimate Analysis**

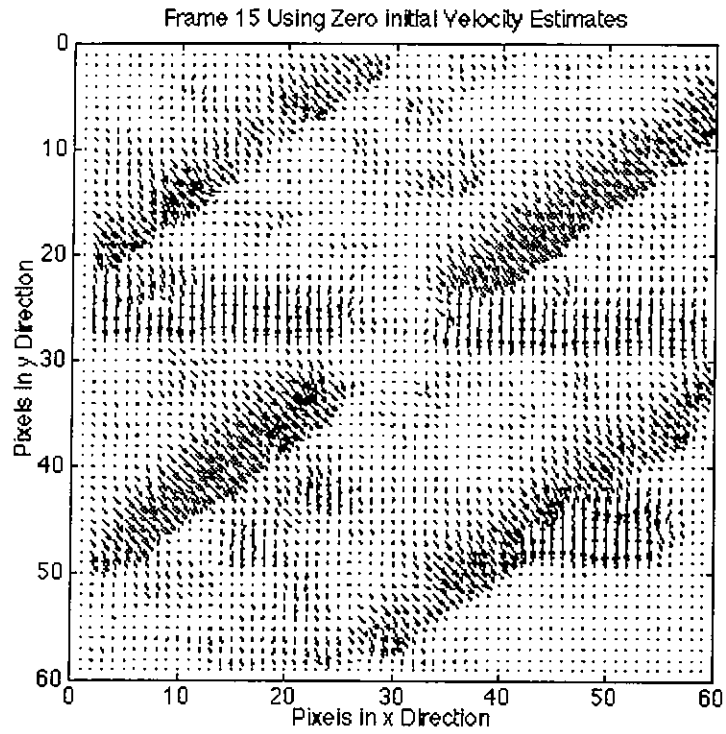


**Figure A.13. Frame 15 of Zero Initial Velocity Estimate Analysis**

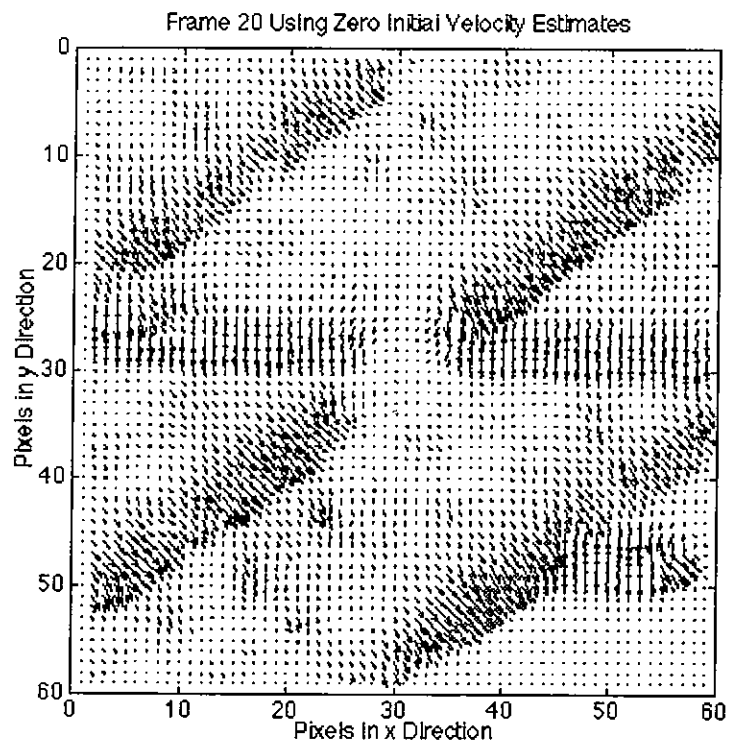


**Figure A.14. Frame 20 of Zero Initial Velocity Estimate Analysis**

## B. Extending the Partial Derivative Estimate

### B.1. Expansion to More than Two Pixel Motion

The estimates of the partial derivatives of intensity ( $I_x$ ,  $I_y$ , and  $I_t$ ) given by Equation (4.11) are not accurate for more than one pixel motion in either component direction. This appendix is provided to expand the estimates of the partial derivatives of intensity to cover more than one-pixel motion. The partial derivatives in Equation (4.11) are calculated using two pixels in each coordinate direction ( $x, y, t$ ).

The central difference equation is used for an expansion to 2 pixel motion.

$$f'(x) = \frac{f(x + \Delta x) - f(x - \Delta x)}{2\Delta x}. \quad (\text{B.1})$$

Figure B.1 represents 3 pixels in the image plane ( $x, y$ ) and 2 pixels in time. For this case, the measurement ( $x, y, t$ ) is actually calculated at the center of the block ( $i, j, k+1/2$ ). Since this is not a pixel location, the partial is applied to the pixel location ( $i, j, k$ ). The one-dimensional central difference Equation (B.4) is averaged over the first three adjacent differences in two frames (six differences total) to estimate the three-dimensional partial derivatives with respect to the image plane coordinates ( $I_x, I_y$ ). The partial derivative of time ( $I_t$ ) is taken as the average of the first 2-pixel central differences between two frames.  $I_t$  is calculated as an average of the 2-pixel central difference because image loading time is significantly less if no more than two frames are used in framewise analysis. Figure B.1 shows pixel measurements as blocks, where the measurement ( $i, j, k$ ) is in the center of the first frame of the block. The partial derivatives of intensity are calculated in Equations (B.2), (B.3), and (B.4)

$$I_x = \frac{1}{2\Delta x} \left( \frac{1}{6} \right) [(I_{i+1,j+1,k} - I_{i+1,j-1,k} + I_{i,j+1,k} - I_{i,j-1,k} + I_{i-1,j+1,k} - I_{i-1,j-1,k}) + (I_{i+1,j+1,k+1} - I_{i+1,j-1,k+1} + I_{i,j+1,k+1} - I_{i,j-1,k+1} + I_{i-1,j+1,k+1} - I_{i-1,j-1,k+1})] \quad (\text{B.2})$$

$$I_y = \frac{1}{2\Delta y} \left( \frac{1}{6} \right) [(I_{i+1,j+1,k} - I_{i-1,j+1,k} + I_{i+1,j,k} - I_{i-1,j,k} + I_{i+1,j-1,k} - I_{i-1,j-1,k}) + (I_{i+1,j+1,k+1} - I_{i-1,j+1,k+1} + I_{i+1,j,k+1} - I_{i-1,j,k+1} + I_{i+1,j-1,k+1} - I_{i-1,j-1,k+1})] \quad (\text{B.3})$$

$$I_t = \frac{1}{\Delta t} \left( \frac{1}{9} \right) [(I_{i+1,j+1,k+1} + I_{i,j+1,k+1} + I_{i+1,j,k+1} + I_{i,j,k+1} + I_{i-1,j+1,k+1} + I_{i+1,j-1,k+1} + I_{i,j-1,k+1} + I_{i-1,j,k+1} + I_{i-1,j-1,k+1}) + (-I_{i+1,j+1,k} - I_{i,j+1,k} - I_{i+1,j,k} - I_{i,j,k} - I_{i-1,j+1,k} - I_{i+1,j-1,k} - I_{i,j-1,k} - I_{i-1,j,k} - I_{i-1,j-1,k})] \quad (\text{B.4})$$

The estimates in Equations (B.2), (B.3), and (B.4) are computationally more expensive than those in the simpler estimates in Equation (4.11) so it is desired to run the experiment so motion does not exceed the one-pixel motion constraint for any two frames in the series.

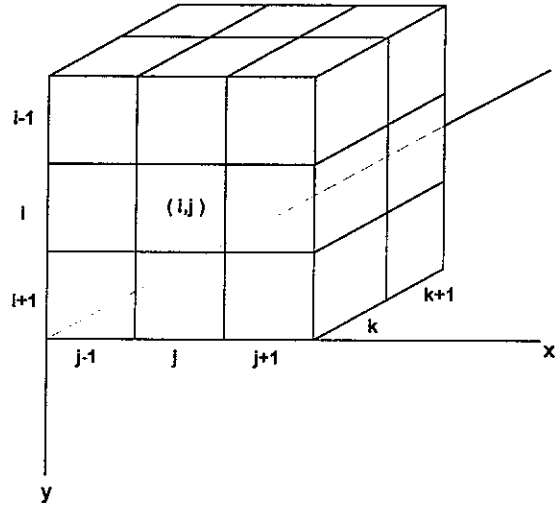
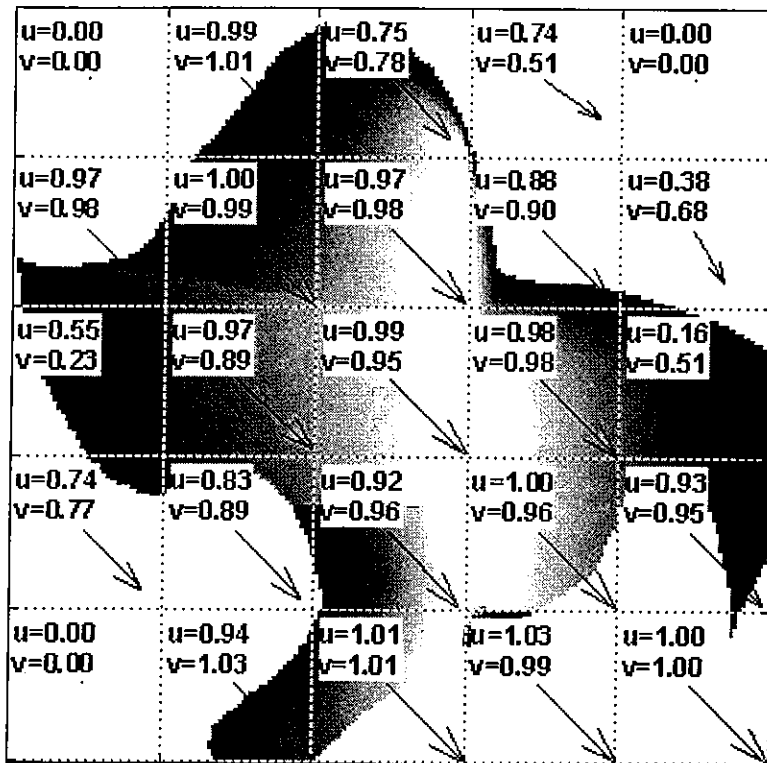


Figure B.1. Expanded Estimation of Partial Derivatives

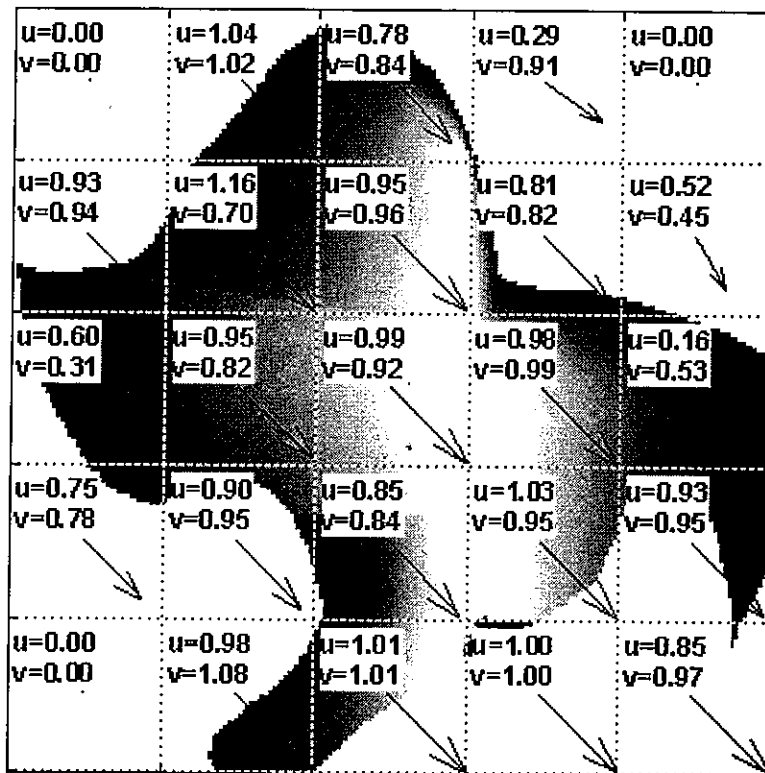
## B.2. Testing the Expanded Partial Derivative Estimates

The expanded central difference estimates were tested for accuracy using the same one-pixel diagonal test series used in Chapter 5. See Figure B.2 for comparison of the forward difference method results from Chapter 5 and the central difference method results from this appendix. Both methods provide similar results.

Next, the central difference method was tested on a diagonal movement of two pixels in both component directions. In this case, the expected value of the component velocities  $(u, v)$  is 2. Figure B.3 shows the results for this two-pixel case. The two-pixel case results show that it is possible to extend the partial derivative estimates to include motion of more than one pixel. This case was tried with the estimation partials estimated in Equation (4.11) and provided inaccurate results. However, additional analyses should be performed to determine which higher order extension works best for the data set given. Note that the PASDE data set did not require this estimate extension.

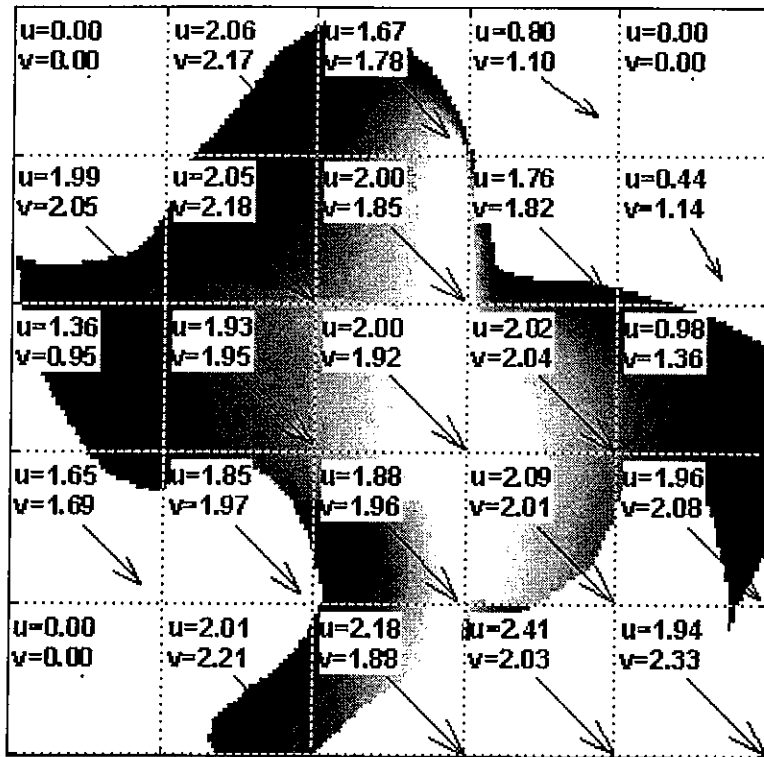


a. Results of Forward Difference from Chapter 5



b. Results of Extended Central Difference

Figure B.2. Comparison of Results from the Chapter 5 Forward Difference Method and from the Appendix B Central Difference Method



Results of Central Difference with a Two Pixel Motion

Figure B.3. Extended Partial Derivative Component Velocity Results